

Testing the correlation between bending angle and polarization properties of bent radio galaxies

S. VANDERWOUDE ,^{1,2} E. OSINGA ,^{2,3} B. M. GAENSLER ,^{4,2,1} J. L. WEST ,⁵ AND R. J. VAN WEEREN ,³

¹*David A. Dunlap Department of Astronomy and Astrophysics, University of Toronto, Toronto, ON M5S 3H4, Canada*

²*Dunlap Institute for Astronomy and Astrophysics, University of Toronto, Toronto, ON M5S 3H4, Canada*

³*Leiden Observatory, Leiden University, PO Box 9513, NL-2300 RA Leiden, The Netherlands*

⁴*Department of Astronomy and Astrophysics, University of California, Santa Cruz, Santa Cruz, CA 95064, USA*

⁵*Dominion Radio Astrophysical Observatory, Herzberg Astronomy and Astrophysics, National Research Council Canada, P.O. Box 248, Penticton, BC V2A 6J9, Canada*

ABSTRACT

The bending of radio galaxies in galaxy clusters is expected to be caused by interactions with the local environment. The physical processes responsible for jet bending, and their influence on the polarization properties of radio galaxies, remain poorly understood, leading to the question of whether jet properties in bent radio galaxies differ from those in linear radio galaxies. Using a sample of 24 polarized bent radio galaxies, observed with the Karl G. Jansky Very Large Array at 1–2 GHz, we test for correlation of bending angle with polarization parameters measuring Faraday rotation, intrinsic fractional polarization, and Faraday rotation dispersion, used here as a measure of turbulence along the line of sight. We find no statistically significant correlations. At the spatial resolution of our dataset (3–46 kpc, median 18.4 kpc), our results indicate that we are primarily probing larger-scale intracluster medium effects not related to bending angle. The absence of a statistically significant correlation suggests that bent radio galaxies are reliable probes of intracluster magnetic fields, because their intrinsic properties do not appear to introduce systematic biases into measured polarization parameters. We do detect a preference for source magnetic field vectors to align with the direction of jet bending. Finally, we estimate that the POSSUM and SKA surveys will contain $\gtrsim 300$ and $\gtrsim 1000$ polarized radio galaxies, respectively, providing large future samples with a range of bending angles and similar redshift distribution and number of beams per source as in our sample, enabling our results to be tested with greater statistical power.

Keywords: Radio galaxies, polarimetry, astrophysical magnetism

1. INTRODUCTION

Radio galaxy morphologies are widely varied, and it is generally assumed that a bent or disturbed radio galaxy morphology results from the interaction between the galaxy’s jets and its surrounding environment. The typical model for a radio galaxy consists of two collimated, synchrotron-emitting jets of plasma ejected to very large distances from opposite sides of a central active galactic nucleus (AGN) of a host galaxy. With no interactions with the surrounding environment, the jets should propagate out linearly. However, the presence of density variations in the intracluster medium (ICM) in galaxy clusters and ram pressure from the motion of radio galaxies through the ICM can cause radio galaxy jets to bend and their lobes to be distorted, resulting in a variety of morphologies (Begelman et al. 1979; Jones & Owen 1979; Vallee et al. 1981; Hardcastle et al. 2005;

Freeland et al. 2008; Morsony et al. 2013; Garon et al. 2019; O’Dea & Baum 2023). Under this assumption, bent radio galaxies have been used to search for and identify galaxy clusters (e.g. Blanton et al. 2000; Wing & Blanton 2011; Banfield et al. 2016; Paterno-Mahler et al. 2017).

Radio galaxies are broadly categorized using the Fanaroff-Riley (FR) classification system (Fanaroff & Riley 1974), where FRI galaxies are brighter at their cores and decrease in brightness with distance from the central AGN, while FRII galaxies are brighter in their lobes and fainter closer to the AGN. Bent radio galaxies require additional classifications. These include wide-angle tail (WAT) and narrow-angle tail (NAT) bent radio galaxies (often grouped together under the broader classification of head-tail radio galaxies; Rudnick & Owen 1976; Owen et al. 1979; Blanton et al. 2000; De-

hghan et al. 2014; Missaglia et al. 2019; Pal & Kumari 2023). Other classifications include “winged”, or X- and Z-shaped, radio galaxies (Yang et al. 2019; Bera et al. 2020, 2022), and double-double radio galaxies (Nandi & Saikia 2012; Mahatma et al. 2019), while some radio galaxies have morphologies that are unable to be classified (Sasmal et al. 2022; Bera et al. 2024)

Total intensity statistical studies of bent radio galaxies and their environments have been carried out both at low-to-intermediate redshifts (Owen & Rudnick 1976; Sakelliou & Merrifield 2000; Blanton et al. 2001; Freedland et al. 2008; Wing & Blanton 2013) as well as high redshifts (Golden-Marx et al. 2019, 2021, 2023). Additional works spanning a wider redshift range have further expanded this picture (O’Brien et al. 2018; de Vos et al. 2021; Morris et al. 2022; Vardoulaki et al. 2021, 2025; Mingo et al. 2019; Garon et al. 2019; van der Jagt et al. 2025). Despite this extensive body of work in total intensity, no statistical polarization studies of bent radio galaxies have been conducted to date. If radio galaxy morphology is related to the magnetic properties of the jets (e.g., magnetic field strength or geometry), we might expect to see a correlation between the bending angle of a radio galaxy and polarization parameters that probe these environmental variables, such as Faraday rotation measure (RM), polarized fraction (p), and depolarization, potentially due to turbulence in the ICM. In addition, understanding the origin of RM structures seen across radio galaxies jets and lobes (e.g. Guidetti et al. 2011; Sebokolodi et al. 2020) is important for cluster magnetism studies. Determining whether the observed RM structure is related to the ICM foreground or whether it is intrinsic to the radio galaxy itself has implication for inferring magnetic field properties of the ICM (Rudnick & Blundell 2003; Ensslin et al. 2003; O’Sullivan et al. 2013).

In this paper, we investigate the question of whether the degree of bending of radio galaxies is correlated with measured polarization properties, using bent radio galaxies in cluster environments, observed with the Karl G. Jansky Very Large Array (VLA) in L-band (1–2 GHz). We organize the paper as follows. In Section 2 we describe our data and our method of sample selection. In Section 3 we outline our method of analysis, including spectral extraction and modeling. We present the results of our analysis in Section 4, and we discuss the implications of these results and potential for future work with upcoming surveys in Section 5. The paper is summarized in Section 7. Throughout this work, we assume a flat Λ cold dark matter (Λ CDM) cosmology of $H_0 = 70 \text{ km s}^{-1} \text{ Mpc}^{-1}$, $\Omega_m = 0.3$, and $\Omega_\Lambda = 0.7$ (see Planck Collaboration et al. 2020).

2. DATA AND SAMPLE SELECTION

2.1. Calibration and Imaging

We analyze L-band (1–2 GHz) observations of radio galaxies in galaxy clusters obtained with the Karl G. Jansky Very Large Array (VLA) and first presented by Osinga et al. (2022). The clusters were selected through the Sunyaev–Zel’dovich (SZ) effect, which is insensitive to cluster dynamical state and therefore provides a close-to-unbiased, mass-limited catalogue of clusters (e.g., Andrade-Santos et al. 2017). From the Planck Early Sunyaev–Zel’dovich (PESZ) catalogue (Planck Collaboration et al. 2011), we included all clusters at redshift $z < 0.35$ and declination $> -30^\circ$, observable with the VLA¹. This yielded 102 clusters. To this set, 24 clusters were added from the first and second Planck SZ source catalogues (Planck Collaboration et al. 2015, 2016) that met the same redshift and declination criteria and for which VLA L-band observations were available. In total, 126 clusters were targeted.

The resulting sample has a slightly higher mean M_{500} (the total mass enclosed within a radius R_{500} , where the mean density is 500 times the critical density of the Universe at the cluster redshift) of $5.7 \times 10^{14} \text{ M}_\odot$ (standard deviation $2.1 \times 10^{14} \text{ M}_\odot$) compared to the parent PESZ sample in the same redshift range (mean $4.3 \times 10^{14} \text{ M}_\odot$, standard deviation $1.8 \times 10^{14} \text{ M}_\odot$). While this difference reflects the availability of VLA data, it is not expected to introduce major additional selection biases.

Each cluster was observed for approximately 40 minutes, giving a typical root-mean-square (rms) noise level of $20\text{--}30 \mu\text{Jy/beam}$ in Stokes I near the field center. Two observations were excluded from further analysis due to severe imaging artefacts, leaving 124 usable clusters. The final images have angular resolutions ranging from 6.2 to 11.9 arcsec, restored to a uniform synthesized beam across frequency.

The data were calibrated by Osinga et al. (2022) using the Common Astronomy Software Application (CASA; McMullin et al. 2007). The analysis of Perley & Butler (2017) was used to set the flux scale, 3C138 and 3C286 were used for polarization calibration, and 3C147 was used for on-axis leakage correction.

Each galaxy cluster was observed with 16 spectral windows over 1008–2032 MHz, each with a bandwidth of 64 MHz. In each spectral window, the first 6 MHz and the last 10 MHz were removed due to low quality. The spectral windows were then averaged to 6 frequency channels with 8 MHz channel width. Spectral window 8 was lost

¹ Correcting a typographical error in Osinga et al. (2022), we note that the declination cut is -30° , not 40°

to radio frequency interference (RFI) in all cases, leaving 90 frequency channels and a total bandwidth of 1008 MHz for each observation. Additional RFI detection with *AOflagger* (Offringa et al. 2012) flagged individual channels in individual observations. All calibration and imaging was performed by Osinga et al. (2022), and a more detailed description of the process can be found therein, as well as the final images of all 124 galaxy clusters.

After imaging, all channels in the Stokes *IQU* data cubes for each observation were convolved to the resolution of the lowest frequency channel of that observation, using a circular synthesized beam. In each case, the galaxy cluster was observed toward the center of the primary beam. The largest angular extent of any galaxy in the clusters is ~ 4.4 arcmin. This is sufficiently smaller than the 30 arcmin FWHM of the primary beam, and therefore we do not expect the off-axis leakage to vary significantly across our sources. Stokes *QU* off-axis leakage levels are expected to be $\sim 1\%$ (Jagannathan et al. 2017) at the full width half maximum (FWHM) of the primary beam. Thus, no correction for off-axis leakage was applied.

Unexpected flux variations between spectral windows were observed by Osinga et al. (2022) in all observations after calibration. They corrected for this by fitting a power law to the brightest sources in each observation and deriving spectral window-specific correction factors which were then applied to each of the Stokes *IQU* cubes. We apply these same correction factors to the data to correct for the flux variations in the same manner.

2.2. Sample Selection

The goal of this work is to probe for a correlation between the degree of bending of radio galaxy jets and the galaxy's magnetoionic environment. We begin with the Osinga et al. (2022) catalogue and identify all extended sources (resolved such that it is larger than at least 3 synthesized beam widths) that show some detectable polarization at any location across the source. This yields 156 radio galaxies. From this initial set of radio galaxies we then apply the following requirements:

- An optical host galaxy with redshift has been identified in the Legacy Survey (Dey et al. 2019), or in Pan-STARRS (Chambers et al. 2019) for fields outside of the Legacy survey coverage. This reduces the sample to 114 radio galaxies.
- Comparison of the host galaxy redshift (z_g) and cluster redshift (z_c) show that the galaxy is a cluster member and not background or foreground to

the cluster. Following Osinga et al. (2022), we determine a galaxy to be a cluster member if both $z_c - (z_g + \delta z_g) \leq 0.04(1+z)$ and $(z_g - \delta z_g) - z_c \leq 0.04(1+z)$ are satisfied, where δz_g is the error associated with the host galaxy redshift. This reduces the sample to 60 radio galaxies.

- Radio galaxy morphology is generally discernible. Any object where it is not clear which components are physically associated with a single radio galaxy and which components are randomly associated (projected nearby but not physically local to each other) is rejected. This leaves us with a final sample of 48 radio galaxies.

The resulting sample of 48 radio galaxies covers 35 galaxy clusters. The clusters spanned by our sample cover a mass (M_{500}) range of $\sim 2\text{--}12 \times 10^{14} M_\odot$, with a mean of $5.8 \times 10^{14} M_\odot$ and a standard deviation of $2.3 \times 10^{14} M_\odot$. The mean, median, and standard deviation are the same, or nearly the same, as those of the larger Osinga et al. (2022) sample. An Anderson-Darling test shows no significant difference between the M_{500} distributions of the two samples.

For each galaxy in our sample, we then calculate a bending angle, θ , from the data following the same method as van der Jagt et al. (2025). van der Jagt et al. (2025) used a subsample of the Osinga et al. (2022) data to probe the correlation between bending angle and location in projected cluster-centric distance-velocity phase space of the radio galaxies. They measured a bending angle for 109 radio galaxies with varying degrees of bending by calculating the angle between the lines connecting the host galaxy position and the two brightest peaks not coincident with the host position. Following the approach of Garon et al. (2019), we do not provide per-source uncertainties on bending angle, since these are dominated by projection effects and structure in the radio emission and can only be characterized statistically across large samples. As Garon et al. (2019) discuss in more detail, the uncertainties scale with angular size and cannot be robustly assigned to individual sources.

Approximately 10% of our sample of radio galaxies are brightest cluster galaxies (BCGs), with bending angles ranging from 32° to 72° ; notably, none of these sources are NATs ($>90^\circ$) or completely straight ($\sim 0^\circ$) sources. We also find no dependence of bending angle on whether the galaxy is a BCG, nor any correlation between bending angle and jet power (calculated at 1.4 GHz).

The angular resolutions of the sample range over $6.2\text{--}11.9$ arcsec. The sample has redshifts $0.023 \leq z \leq 0.318$ and bending angles $1.7^\circ \leq \theta \leq 180^\circ$, where 0° corresponds to a perfectly linear galaxy and increasing θ in-

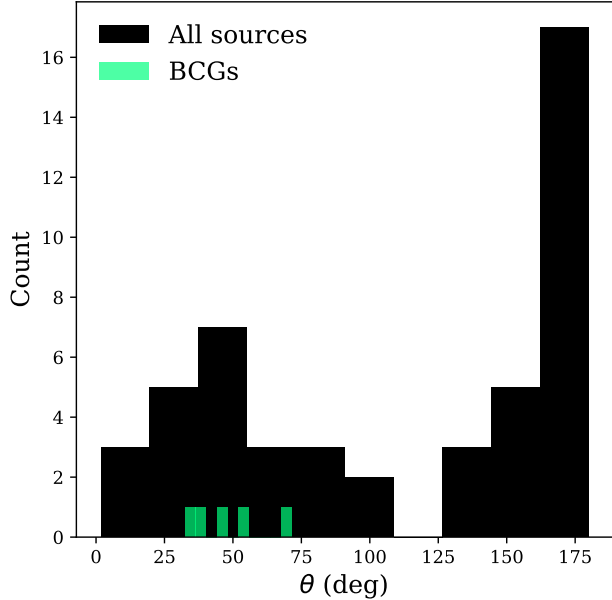


Figure 1. Distributions of bending angles for our sample of 48 radio galaxies. The distribution of bending angles for the BCG galaxies are overlaid in green.

dicates increasing bending. We plot the distribution of bending angles in Figure 1. The peak at 180° is due to head-tail sources where the individual jet/lobe structures are not resolved, and for which we manually set the bending angle to 180° . Cutouts of the total intensity multi-frequency synthesis (MFS) images of the final sample are shown in Figure 2, with the 10σ contours shown in red and the position of the host galaxy indicated by the cyan markers. Note that the images are rotated such that the bending angle is pointing toward the top of the page. The direction of North through East in RA and Dec coordinates is shown by an arrow in each cutout.

We note that our sample is subject to a selection effect, described in Appendix A of Osinga et al. (2025), who analyze the same dataset as Osinga et al. (2022). All of the observations of the galaxy clusters that contain our sources have a common finite field of view of 30 arcmin at 1.5 GHz, leading to a correlation between the projected distance of a source from its cluster center and redshift (see Figure A.1 of Osinga et al. 2025). Since at lower redshift we are biased toward galaxies with smaller projected distances to their cluster center, this may potentially bias our results. We investigate this selection effect in more detail in Section 4.2.

3. POLARIZATION MEASUREMENT AND ANALYSIS

We obtained Stokes IQU spectra for each of our sources on which we performed our analysis. Due to the range in angular and physical resolution of our sample, we chose to integrate over the entire jet/lobe structure as an attempt to mitigate resolution effects and maintain a consistent comparison between sources. We defined the region within which we integrated the intensity as the 10σ contour of the source in the total intensity MFS image. We chose a 10σ contour to balance including a significant fraction of the source intensity with minimizing the impact of noise. Because we integrate all pixels within the contour, and polarized intensity is typically much lower than total intensity, pixels in Stokes QU outside of the 10σ contour will most likely be unpolarized and can introduce additional noise into our integrated spectrum. We used a similar method as Golden-Marx et al. (2023), who investigated the relationship between environment and bending angle of bent radio galaxies in high-redshift clusters in total intensity using a 10σ contour for intensity integration.

To obtain the per-channel integrated flux density, we placed the 10σ contour from the total intensity image on each channel of the Stokes IQU data cubes and integrated all pixels within the boundary of the contour. The per-channel uncertainty was calculated as the rms of a 30×30 pixel off-source region (the same region in each channel) multiplied by the square root of the number of independent beams sampled by the integration.

There were three general cases that each required different methods of integrating the flux within the 10σ contours:

1. Radio galaxies where the individual jet/lobe structures have separate 10σ contours (e.g., J111140 + 404706 in Figure 2). In such cases, we integrated the pixels within each contour both individually and all together. This gave us spectra from the individual lobes as well as from the full source, so that, if each lobe is polarized but with different properties, we could analyze the individual lobe spectra as well as the combined spectrum (similar to the source being unresolved within the synthesized beam). In our sample, there are 4 sources that fall into this category, and they are indicated by an “SL” (“Separate Lobes”) in Figure 2.
2. Radio galaxies where the 10σ contour encloses the entire source (e.g., J084300 + 361744 in Figure 2). In such cases, we defined a bisector line that separated the two jet/lobe structures, passing through the position of the optical host and following a path of minimum flux between the two structures. We did this visually, guided by higher level con-

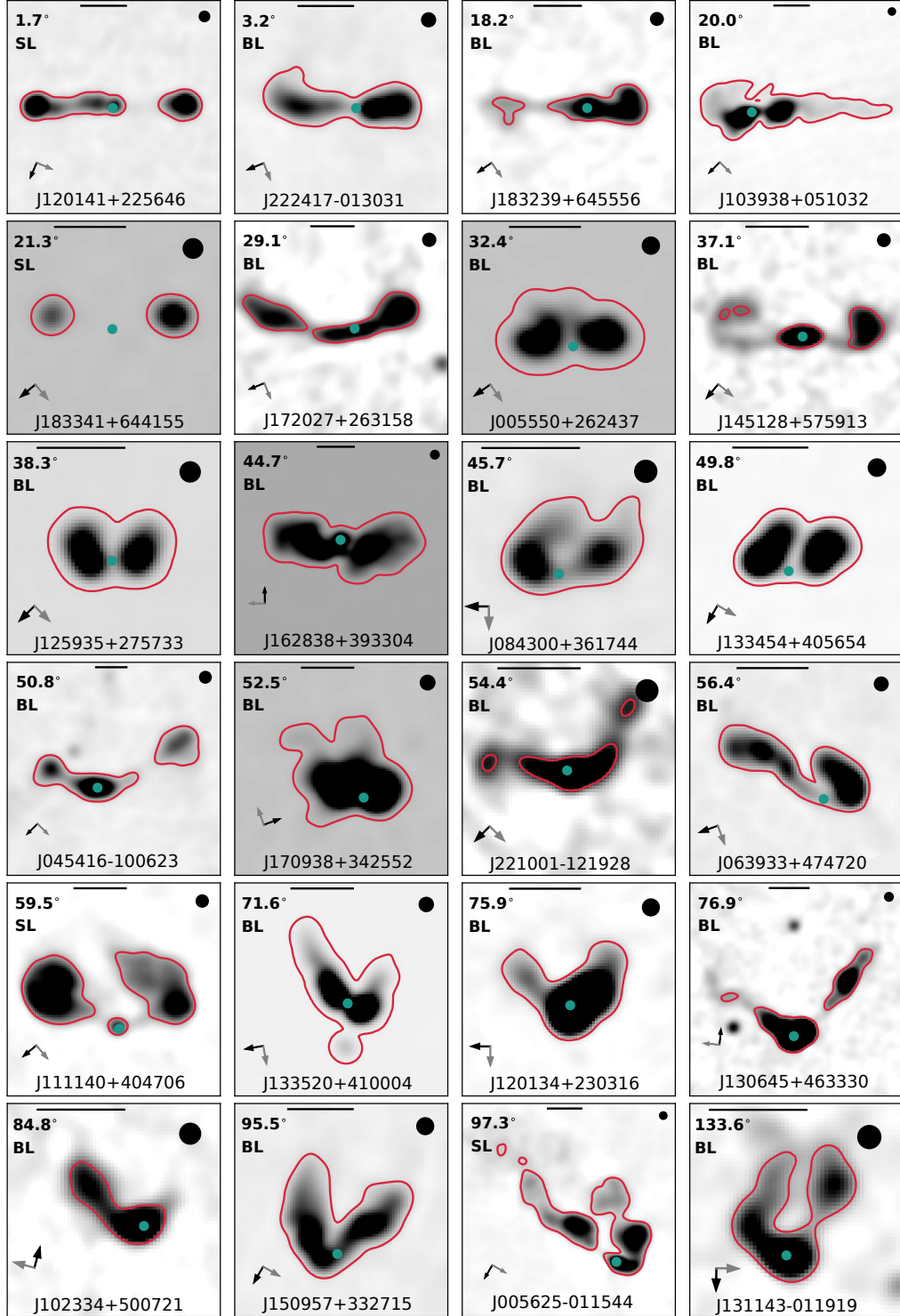


Figure 2. Cutouts of the Stokes I MFS images of the first 24 radio galaxies in our sample, ordered by increasing bending angle. The cutouts have been rotated such that the bisector is pointing approximately toward the top of the page. The grayscale maps total intensity, and the red outlines indicate the 10σ contour lines in the image. The black arrow indicates the direction of increasing declination (north), and the gray arrow points east. The position of the host galaxy is indicated by a cyan circle. The black circles in the top right of the cutouts show the synthesized beam area and the black line at the top of the cutouts span 30 arcsec. The bending angles are noted in the top left corners, with the source integration method (“SL”, “BL”, or “FS”) indicated below (see text in Section 3 for a description of these integration methods). Sources with bending angle 180° are in brackets to indicate that these are head-tail sources for which we are not able to resolve the individual jet/lobe structures.

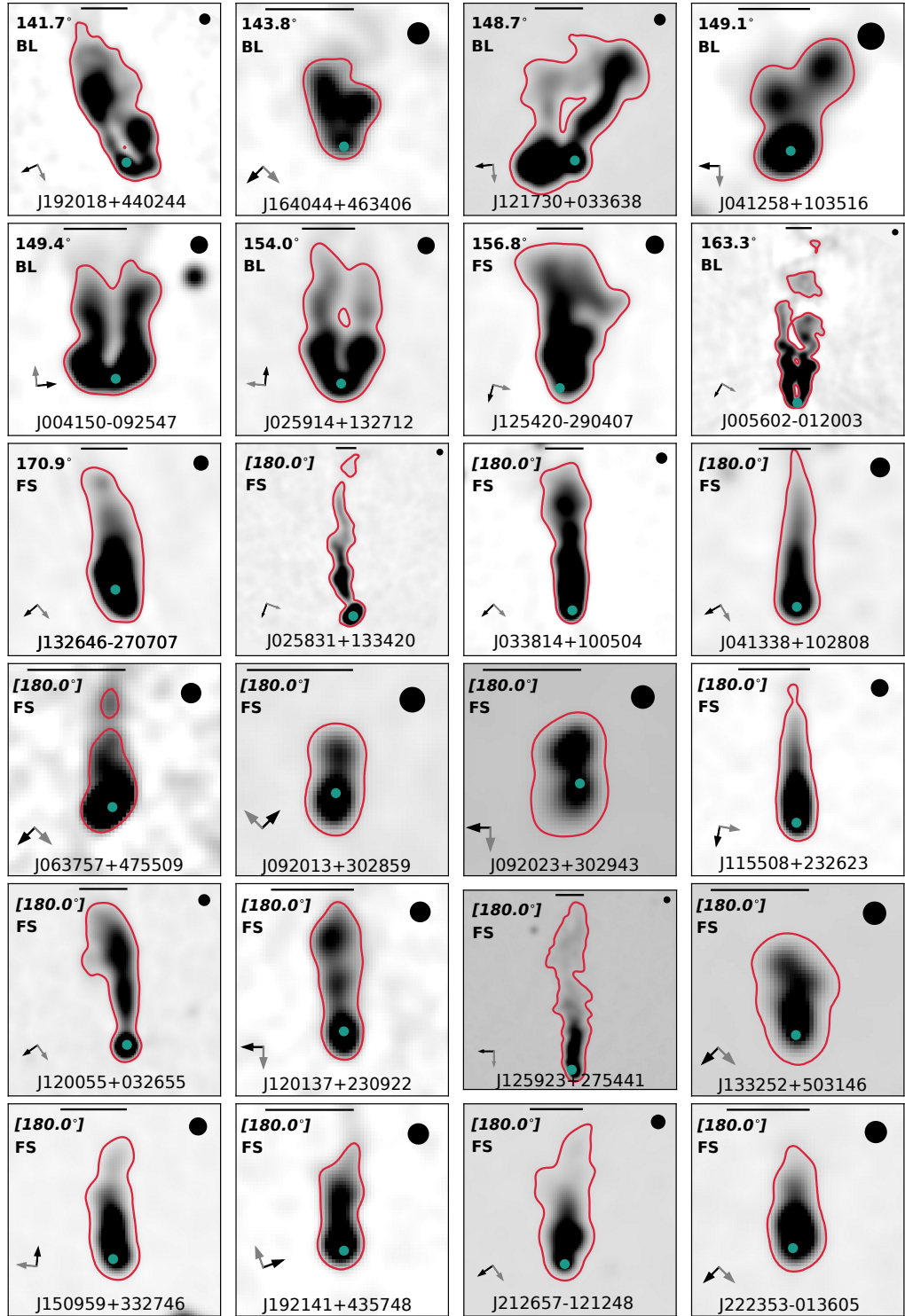


Figure 2. continued. The remaining 24 radio galaxies in our sample.

tour lines (10σ , 20σ , and 25σ). We then integrated all pixels on each side of the bisector line as well as all pixels within the 10σ contour, which again gave us spectra from the individual lobes as well as from the full source. In our sample, there are 27 sources that fall into this category, and they are indicated by a “BL” (“Bisector Line”) in Figure 2.

3. Radio galaxies where the individual jet/lobe structures could not be resolved (see Section 2.2), or where to draw a bisector line between the two jet/lobe structures is not obvious. This includes sources with a bending angle of 180° (e.g., J041338 + 102808 in Figure 2), or sources with a large bending angle and no clear indication from the 10σ contour where the two jets separate (e.g., J125420 – 290407 in Figure 2). In these cases we only integrated all pixels inside the 10σ contour. These sources were compared only to the full-source integrated spectra from the other sources in the sample. In our sample, there are 17 sources that fall into this category, and they are indicated by an “FS” (“Full Source”) in Figure 2.

3.1. Physical resolution effects

The radio galaxies in our sample span a range of redshifts and angular sizes. We first wanted to determine whether we are able to compare our sample at their original resolutions, without experiencing effects due to variation in physical and angular resolutions. To do this, we selected a subsample of radio galaxies with clearly resolved jet/lobe structures as well as one radio galaxy where the jets/lobes were not individually resolved (a source with bending angle 180°). We degraded the resolution from that of the original observation (7–10 arcsec) to 30 arcsec, at which point the jet/lobe structures in each of the observations became fully unresolved and began to merge with each other. We performed 1D RM synthesis on the spectra of each source at each resolution using the RM-Tools² software package (*v1.4.6*; Purcell et al. 2020) to obtain the peak RM and the polarized fraction, p .

We found that, up to a resolution where the jet/lobes structures do not merge (typically \sim 15–20 arcsec), the measured RMs typically remained consistent within uncertainty, and the measured polarized fraction varied by \sim 1% in the more resolved galaxies and by \lesssim 10% in the 180° galaxy. This is in agreement with resolution testing done by Sebokolodi et al. (2020) on Cygnus A, in which they found that beyond a certain resolution, fractional

Table 1. Summary of statistics of sample subsets.

Subset	Count (%)	Statistics
Total	48 (100)	50% polarized
$\theta = 180^\circ$	15 (31)	53% polarized
$\theta \neq 180^\circ$	33 (69)	21% one lobe polarized 15% both lobes polarized 12% full source polarized
Unpolarized	24 (50)	75% at $R < R_{500}$ $p: 0.02\text{--}6\%, \mu = 1\%, \sigma = 1\%$
Polarized	24 (50)	58% at $R < R_{500}$ $p: 0.02\text{--}14\%, \mu = 3\%, \sigma = 3\%$

polarization along a given line-of-sight varied little with decreasing resolution (see Figure 7 of Sebokolodi et al. 2020). These results suggested that physical resolution does not have a strong effect on our results, and so we performed all further analysis at the original angular resolutions of each observation.

3.2. RM synthesis

We performed 1D RM synthesis on the integrated spectra of all of our sources. We found that 24 out of 48 (50%) of the radio galaxies were polarized above a signal-to-noise in polarization, S/N_{pol} , threshold of 6 in at least one lobe or over the full source. We adopted a threshold of $S/N_{\text{pol}} = 6$ to ensure robust polarization detections, as lower S/N values can be affected by statistical bias and uncertainty in polarization measurements (Macquart et al. 2012). Of the 15 total sources with $\theta = 180^\circ$ (sources where we are unable to resolve two distinct jets/lobes), 8 (53%) were polarized. Of the 33 total sources with two distinct jets/lobes, 7 (21%) had only one polarized lobe, 5 (15%) were polarized in both lobes, and 4 (12%) were polarized only when integrating all pixels inside the 10σ contour. We also found that 18 of the 24 (75%) unpolarized sources had a projected distance to the cluster center $R < R_{500}$, where R_{500} is the radius enclosing an overdensity of 500 at the cluster redshift. Of the polarized sources, 14 out of 24 (58%) had $R < R_{500}$. This agrees with the findings of Osinga et al. (2022), who found increasing depolarization with decreasing distance to the cluster center. The measured fractional polarization of the unpolarized (polarized) sources ranges over 0.02–6% (0.02–14%), with a mean of 1% (3%) and standard deviation of 1% (3%). We summarize these subsamples and their statistics in Table 1.

We also performed 3D RM synthesis on cutouts of each of our sources using the RM-Tools package. This re-

² <https://github.com/CIRADA-Tools/RM-Tools>

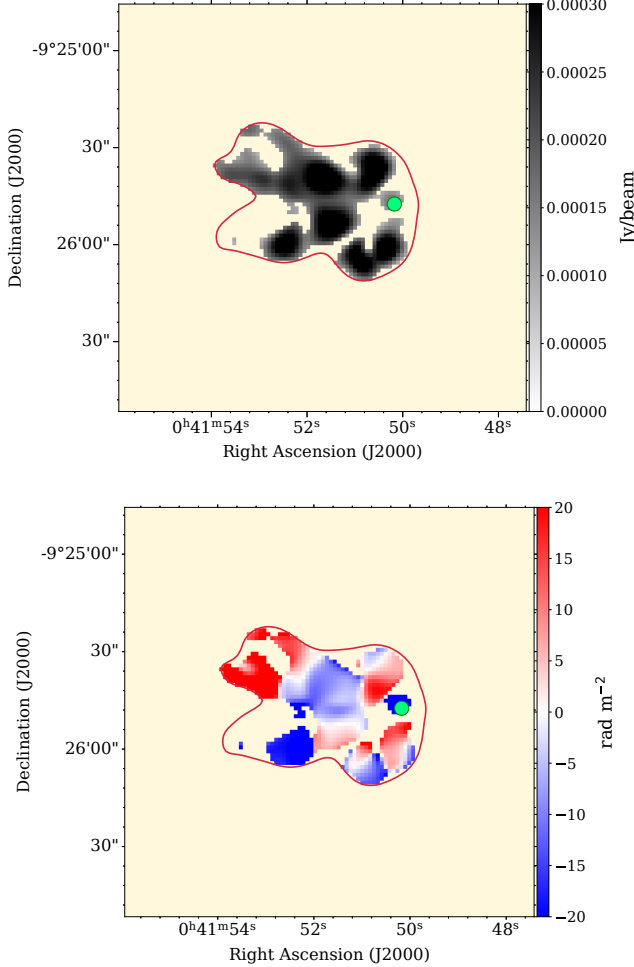


Figure 3. Example 2D maps of polarized intensity (top) and RM (bottom) for source J004150 – 092547, derived from 3D RM synthesis. The 10σ contours from the Stokes I MFS image is shown in red, and the position of the host galaxy is indicated by the green circle. Masked pixels are colored light yellow for clarity.

turned continuous 2D maps of several polarization properties, including polarized intensity, RM, S/N_{pol} , and derotated polarization angle (ψ_0). In Figure 3 we show examples of the 2D polarized intensity (top panel) and RM maps (bottom panel) for source J004150 – 092547.

3.3. Modeling the polarized spectra

After extracting the integrated Stokes IQU spectra for each of our sources, we fit the integrated fractional Stokes qu spectra (Q/I , U/I) with a model that describes depolarization due to an external, non-emitting, turbulent Faraday screen (isotropic turbulence). With this model, the complex fractional Stokes qu function, $p(\lambda)$, is defined as

$$p(\lambda) = p_0 \exp(2i[\psi_0 + \text{RM}\lambda^2]) \exp(-2\sigma_{\text{RM}}^2\lambda^4), \quad (1)$$

where p_0 is the intrinsic fractional polarization of the emission, ψ_0 is the derotated polarization angle of the emission, RM is the total Faraday rotation experienced by the polarized emission along the line-of-sight, and σ_{RM} is the dispersion in RM. This model is adapted from Burn (1966) and Sokoloff et al. (1998), and has been used in several previous studies (e.g., Anderson et al. 2015; O’Sullivan et al. 2012, 2017; Ma et al. 2019; Osinga et al. 2025).

We fit our data with this model because Osinga et al. (2022) showed that this model was an accurate fit to $\sim 75\%$ of their data (of which our data are a subset), and 88% of our sample are among those well fit by the model. We note that Osinga et al. (2022) fit individual components identified by a source finder, while we fit the lobe- and source-integrated spectra (which may include multiple components), making a direct comparison between the fits difficult. We fit all source spectra with a single model to limit the number of free parameters and to simplify the analysis and comparison between sources. This approach minimized the risk of overfitting the data while also maintaining consistency across the data set.

To perform the model fitting, we used the Stokes QU fitting module in **RM-Tools**. The module uses multinest fitting and the **dynesty** sampler to explore a defined parameter space. We defined the parameter space for the model fit as follows: p_0 over 0.001 – 1 , Ψ_0 over 0° – 180° , RM over -1000 to $+1000$ rad m $^{-2}$, and σ_{RM} over 0 – 100 rad m $^{-2}$.

3.3.1. Correcting model parameters for redshift

Equation 1 has four free parameters: p_0 , ψ_0 , RM, and σ_{RM} . RM and σ_{RM} have a dependence on redshift that needs to be corrected. The total measured RM from an extragalactic source can be written in terms of the individual contributions:

$$\text{RM} = \text{RM}_{\text{host}} + \text{RM}_{\text{ICM}} + \text{RM}_{\text{IGM}} + \text{RM}_{\text{MW}}, \quad (2)$$

where RM_{host} is the contribution to the total RM from the host galaxy itself, RM_{ICM} is the contribution from the intracluster medium (if the galaxy is located within a galaxy cluster), RM_{IGM} is the contribution from the intergalactic medium, and RM_{MW} is the contribution from the path length through the Milky Way. Any other intervening magnetized plasma will also contribute to the total RM of a source (see Akahori & Ryu 2010 for a more detailed discussion). Upper limits on $|\text{RM}_{\text{IGM}}|$ are estimated to be ~ 1 – 4 rad m $^{-2}$ (Akahori & Ryu 2010; O’Sullivan et al. 2020; Amaral et al. 2021), and so it is not expected to contribute meaningfully to the total source RM due to its relatively small magnitude.

We are interested in the RM from the source and its host environment, and not the contribution from our Galaxy, RM_{MW} . To correct for RM_{MW} , we subtracted the Galactic contribution along the source line-of-sight using the value from the [Hutschenreuter et al. \(2022\)](#) Galactic Faraday sky map, defining the result as RM_{sub} . We then corrected RM_{sub} for redshift dependence using the equation $\text{RM}_{\text{corr}} = \text{RM}_{\text{sub}}(1 + z_c)^2$. We note that this method of redshift correction assumes that the total contribution to the RM from the intergalactic medium (IGM) along the line of sight is negligible with respect to the RM contribution from the ICM.

We corrected the model-fit σ_{RM} for redshift dependence in a similar manner, using the equation $\sigma_{\text{RM,corr}} = \sigma_{\text{RM}}(1 + z_c)^2$. None of our sources were observed along lines of sight near the Galactic plane (all sources are at Galactic latitude $b < -28^\circ$ or $b > +17^\circ$), which likely minimizes the Galactic contribution to the total value of σ_{RM} , and a plot of σ_{RM} versus Galactic latitude shows no obvious correlation. We currently have no way of separating the Galactic contribution to the total σ_{RM} , so this is a potential confounding factor in our analysis ([Leahy 1987](#)). The other model parameters, ψ_0 and p_0 , have no dependence on redshift and required no correction.

4. RESULTS

In this section we present the results of Kendall's rank correlation coefficient (τ) tests between the polarization parameters of the polarized sources and bending angle. We also present the results of tests for coherence in the derotated magnetic field vector angles of the sources, and alignment with the direction of bending.

4.1. Parameters as a function of bending angle

In Figure 4 we present plots of our primary model parameters, $|\text{RM}_{\text{corr}}|$, $\sigma_{\text{RM,corr}}$, and p_0 , as a function of bending angle for the full-source integrated spectra (top row), the individual lobe-integrated spectra (middle row), and, where possible, the lobe ratios (bottom row). We note that when calculating the polarized fraction ratio, if one of the two lobes has $S/\text{N}_{\text{pol}} < 6$, we consider it depolarized and the ratio is set to 0. In this way, sources with only one detected polarized lobe are still assigned a ratio and included in the polarized fraction ratio plot, whereas for $|\text{RM}_{\text{corr}}|$ and $\sigma_{\text{RM,corr}}$ both lobes must be polarized to form a ratio. This results in more data points in the polarized fraction ratio plot than in the $|\text{RM}_{\text{corr}}|$ and $\sigma_{\text{RM,corr}}$ ratio plots.

Each subplot includes the Kendall's τ correlation statistic, τ , and the corresponding P-value for the test. We set an initial stringent P-value threshold of 0.001,

Table 2. Summary of correlation statistics

Parameters	Kendall's τ^a
Full $ \text{RM}_{\text{corr}} $ vs θ	0.1
Lobe $ \text{RM}_{\text{corr}} $ vs θ	0.4
Full σ_{RM} vs θ	0.3
Lobe σ_{RM} vs θ	0.6 ($P = 6 \times 10^{-4}$)
Full p_0 vs θ	-0.01
Lobe p_0 vs θ	-0.007
Lobe RM ratio vs θ	-0.4
Lobe σ_{RM} ratio vs θ	0.2
Lobe p_0 ratio vs θ	-0.09

^a For all tests except lobe σ_{RM} vs θ , we find $P > 0.01$. We use $P = 3.1 \times 10^{-5}$ as the maximum likelihood threshold for a potential correlation.

and, because we are conducting a large number (32) of correlation tests in this work, we also apply a P-value correction to account for the increased chance of a false positives, or the “look-elsewhere” effect ([Algeri et al. 2016](#)). We therefore set the threshold $P = \frac{0.001}{32} = 3.1 \times 10^{-5}$ as the maximum likelihood threshold for a potential correlation.

Figure 4 does not indicate a statistically significant correlation or anti-correlation between any of our parameters and θ . The statistic for the lobe σ_{RM} versus θ ($\tau = 0.6$, $P = 6 \times 10^{-4}$) suggests a relationship between the two parameters, but it does not meet the threshold of our modified P-value for a correlation. We analyze this potential correlation further in Section 4.2. We summarize the Kendall's tau statistics from Figure 4 in Table 2.

As noted in Section 2.2, our sample is a subsample of the data used by both [Osinga et al. \(2022\)](#) and [Osinga et al. \(2025\)](#). [Osinga et al. \(2022\)](#) report increased depolarization (traced by σ_{RM}) as a function of projected distance to the cluster center, and [Osinga et al. \(2025\)](#) identify increased scatter in RM with decreasing distance to the cluster core. The authors attribute this trend primarily to radial variations in electron density and magnetic field strength in the ICM, and their results are consistent with the expectation that denser, more magnetized plasma near the cluster center produces higher RMs ([Govoni & Feretti 2004](#); [Bonafede et al. 2010](#)). Similarly, [van der Jagt et al. \(2025\)](#), who also analyze a subset of the [Osinga et al. \(2022\)](#) data, identify a significant correlation between jet bending angle and R/R_{500} , suggesting enhanced ram pressure closer to the cluster core. In our lobe spectra sample, we find tentative correlations between both $|\text{RM}|$ and R/R_{500} and between bending angle and R/R_{500} ($P = 0.002$ and $P = 0.004$, respectively), though neither meets our modified thresh-

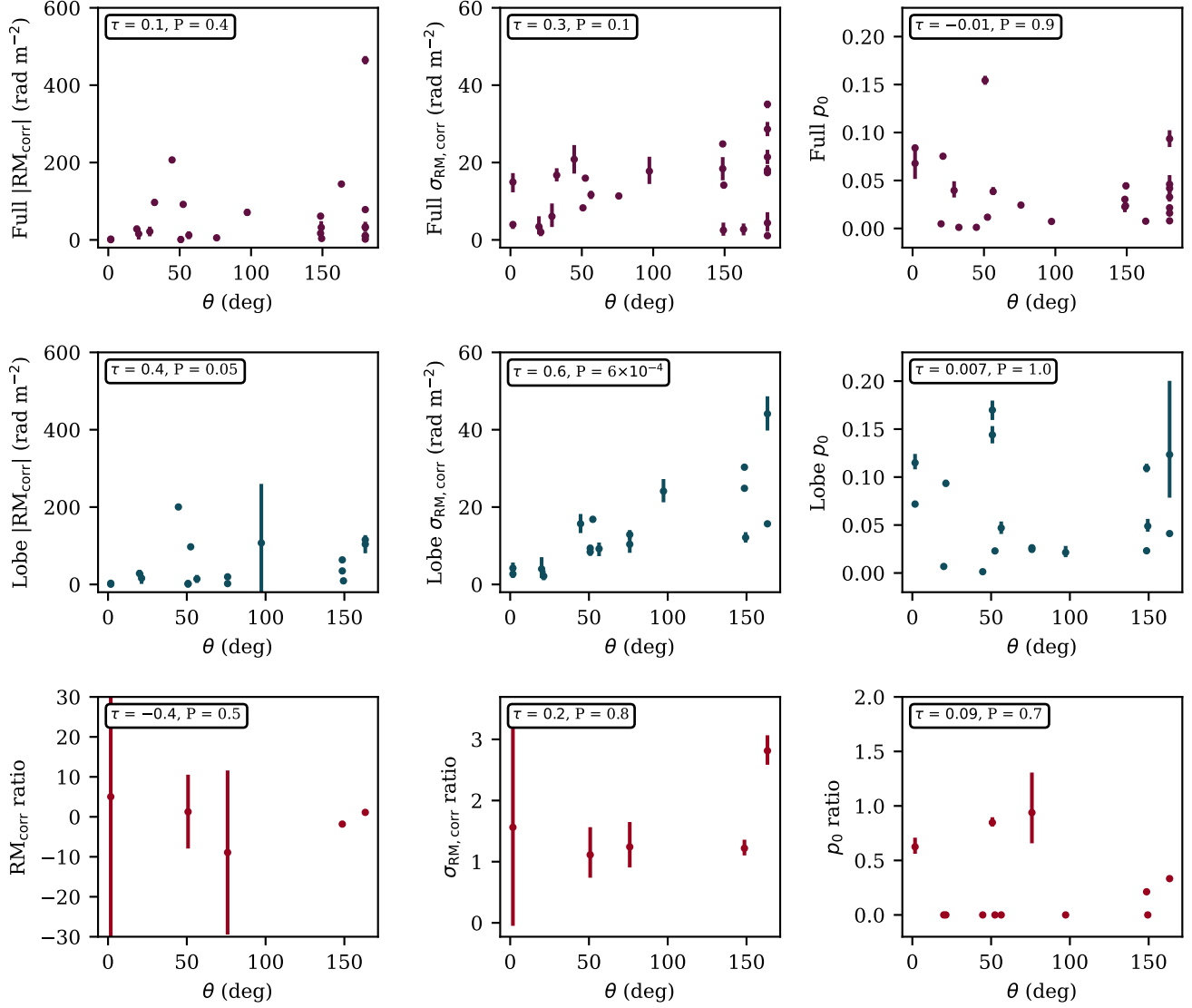


Figure 4. Model parameters versus bending angle for the full-source integrated spectra (top row), the individual lobe-integrated spectra (middle row), and the lobe ratios (bottom row). In each panel, the Kendall's tau correlation coefficient, τ , and corresponding P-value for the data is given in the top left corner. We use a modified P-value of 3.1×10^{-5} as our threshold for correlation.

old for statistical significance. In the full spectra sample, bending angle and R/R_{500} again show a weak trend ($P = 0.003$), but the $|\text{RM}| - R/R_{500}$ relation is statistically insignificant ($P = 0.07$).

4.2. Redshift-limited sample parameters versus bending angle

As described in Section 2.2, our data are subject to a selection effect due to the finite field of view of our observations. We investigate the effects of this selection bias here.

To test whether the redshift-projected distance selection bias noted above has a significant effect on our re-

sults, we take a subset of our sources within a range of redshifts where the distance to the cluster center is not biased by the field of view (i.e., there is no correlation between the two parameters). This is done by selecting sources in the redshift range 0.152–0.301, which yields a reduced sample of 12 radio galaxies. We illustrate this choice in Figure 5, where we plot redshift versus R/R_{500} for our polarized sources, and we include a curve (in black) showing the FWHM of the primary beam of our observations for a cluster with a representative R_{500} of 1 Mpc.

With this reduced sample, we again calculate the Kendall's τ correlation statistics for our three model pa-

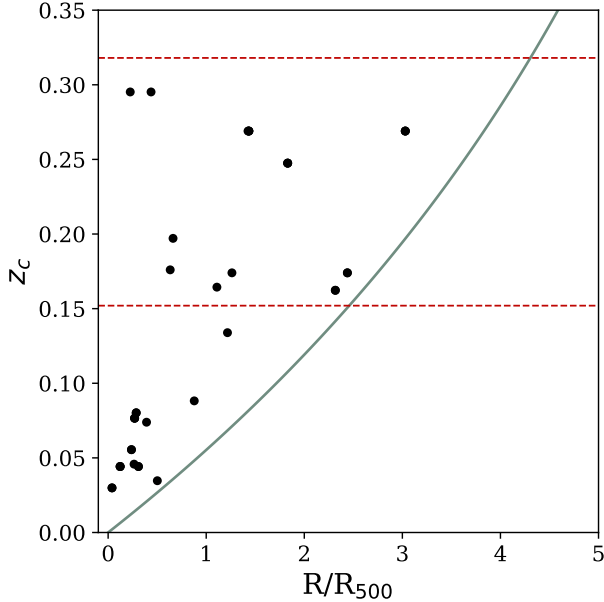


Figure 5. Plot of redshift as a function of the ratio of projected distance to the cluster center and R_{500} . The dashed lines show the redshift bounds within which we select our redshift-limited sample, with which to test the strength of the field-of-view selection effect described in the text on our results. The solid line shows the FWHM of the primary beam of our observations (30 arcsec) for a cluster with a representative R_{500} of 1 Mpc.

rameters, $|\text{RM}_{\text{corr}}|$, $\sigma_{\text{RM,corr}}$, and p_0 , and bending angle for the full-source integrated spectra and the lobe integrated spectra. We do not include the lobe ratio results because the redshift-limited sample contains only 3 sources with two polarized lobes, and is not large enough to calculate any meaningful statistics with.

We present the results in Figure 6. No correlation is found between the polarization parameters and bending angle in the redshift-limited sample. In the case of the lobe $\sigma_{\text{RM,corr}}$ versus bending angle, the possible correlation that we see in Figure 4 is now absent ($\tau = 0.5$, $P = 0.1$). This suggests that the apparent trend in $\sigma_{\text{RM,corr}}$ versus bending angle was influenced by selection effects, although the smaller size of the redshift-limited sample may also play a role. For $|\text{RM}|$ and p_0 , the bias toward sources with a smaller projected distance to the cluster center at smaller redshifts does not appear to have a significant effect on the correlation with bending angle

4.3. Parameters as a function of integrated physical area

For each source, the total integrated physical area is different, depending on the redshift and physical size of each galaxy. Since each spectrum that we model is

from a different integrated physical area, it is important to test whether there is a correlation between physical area and polarization properties, to determine if area is a confounding factor in our tests of correlation with bending angle.

We plot the results in Figure 7, for the full-source integrated spectra (top row), the individual lobe-integrated spectra (middle row), and the lobe ratios where possible (bottom row). The Kendall's tau correlation statistic is calculated for each pair of variables and is included at the top of each subplot. We again use a modified P-value of 3.1×10^{-5} as our threshold for correlation.

The physical area of the synthesized beams in our sample range over ~ 24 – 2400 kpc 2 . The typical integrated physical area of the source spectra, both lobe and full source, is $\lesssim 20\,000$ kpc 2 , and spans ~ 800 – $47\,000$ kpc 2 . No pair of variables meets our threshold for correlation. A Spearman correlation test also shows no correlation between the polarization parameters and integrated physical area.

4.4. Magnetic field vector coherence

After performing 3D RM synthesis, we have a map of the intrinsic magnetic field vector angles for all of our sources. From visual inspection, we find that there appears to be coherence in the vectors in many of the sources, although the coherence can vary between regions (e.g. between a jet and a lobe). To test the coherence of the magnetic field vectors in our sources, we perform a two-sample Anderson-Darling (AD) test on each source, comparing the distribution of the vectors with a randomly drawn distribution of the same sample size.

To obtain reliable results from the AD test, we only consider sources with at least 50 independent magnetic field vectors per source. Additionally, we include only one vector per synthesized beam area to avoid coherence due solely to resolution. To determine which sources meet this criterion, we first mask all pixels in the magnetic field vector map that lie outside of the 10σ contour drawn from the total intensity MFS image. We also mask all pixels inside of the 10σ contour where $S/N_{\text{pol}} < 6$. We then randomly select an unmasked pixel, note the magnetic field vector value at that position, then mask that pixel and all other pixels within one synthesized beam radius. We continue this process until no pixels are left unmasked. The number of independent magnetic field vectors per source from this selection process range over 1–225, with most sources having less than 20 independent vectors. The distribution of the magnetic field vector angle uncertainties lies primarily between 5° and 13° , with $\mu = 9.4$ and $\sigma = 2.5$.

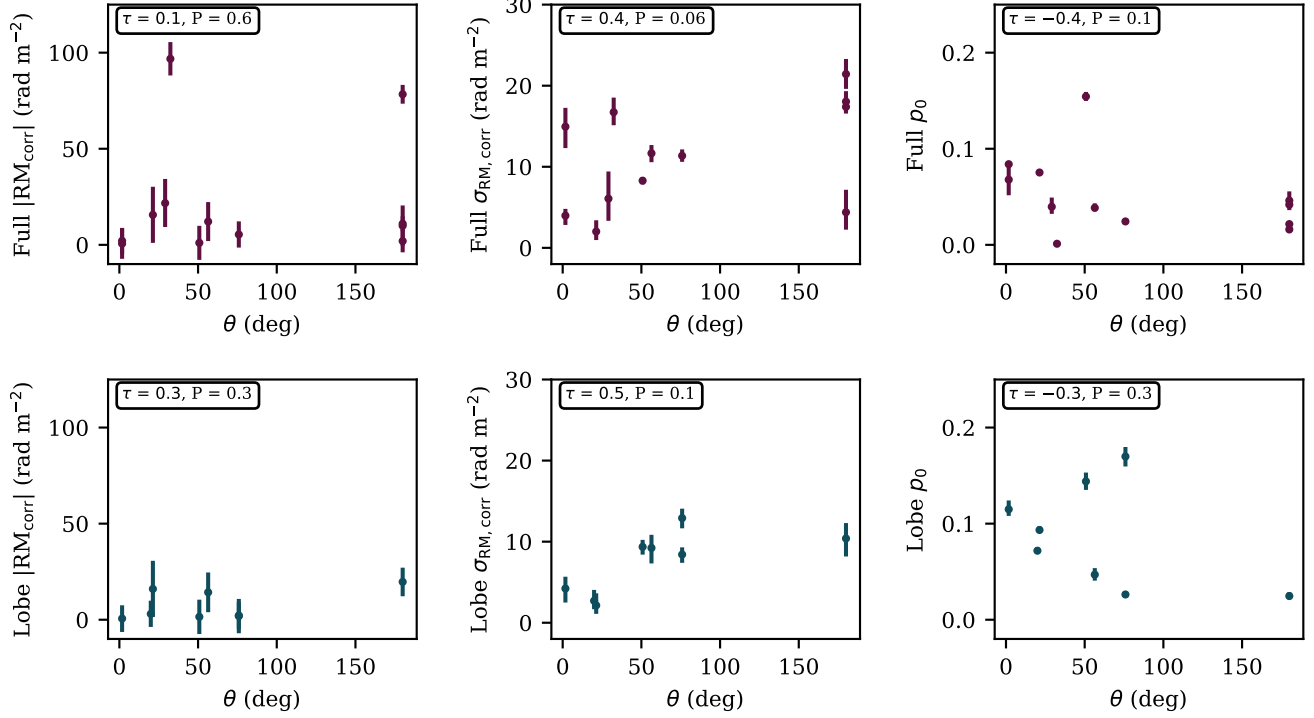


Figure 6. Model parameters versus bending angle for the redshift-limited sample. The full-source integrated spectra are shown in the top row and the individual lobe-integrated spectra are shown in the bottom row. In each panel, the Kendall's tau correlation coefficient, τ , and corresponding P-value for the data are given in the top left corner.

After this selection process, we are left with 8 sources with at least 50 independent magnetic field vectors each. These sources are shown in Figure 8. We note that this figure includes the oversampled magnetic field vectors instead of the re-sampled independent field vectors to provide a clearer visualization. The two-sample AD test statistics are included in the captions below each plot. The results indicate that none of the 8 sources have independent magnetic field vector distributions that are inconsistent with a random field (i.e., the P-value of the AD test is less than 3.1×10^{-5}).

Sources J121731 + 033656 and J005602 – 012003 (Figures 8c and 8e, respectively) have more complicated morphologies as well as having $S/N_{\text{pol}} > 6$ across most of the source. For these sources in particular, the magnetic field vectors appear to follow the morphology of the source, which leads to a variety of different vector angles. While regions of coherence can be identified visually in most of the 8 sources, a more broad distribution of vector angles due to changes in vector orientation across the sources is most likely why the AD test cannot distinguish between the data and random distributions. The two-sample AD test only tests for alignment of the full sample of magnetic field vectors across the entire source, however there may be local alignment that is

not captured by this test. For this reason, in the next section we investigate the local alignment of the magnetic field vectors with the direction of bending of the source.

4.5. Magnetic field vector alignment with the direction of bending

The tendency of the magnetic field vectors in our sources to show some coherence leads to the question of whether the vectors are typically aligned in a common direction. As noted above, in many of the sources in Figure 8, the magnetic field vectors appear to trace the morphology of the radio galaxy. In particular, here we test whether the direction of the magnetic field vectors aligns with the direction of bending in the sources. We perform this analysis on the 24 polarized sources in our sample. We only consider magnetic field vectors derived from pixels with $S/N_{\text{pol}} > 6$, and we select only one pixel per synthesized beam area, using the same selection method as described in Section 4.4.

We define the direction of bending to be the line of peak brightness in total intensity along the source. This is akin to the use of ridgelines, where radio brightness is expected to trace the direction of fluid flow in a radio galaxy (e.g., [Perucho et al. 2012](#); [Vega-García et al. 2019](#);

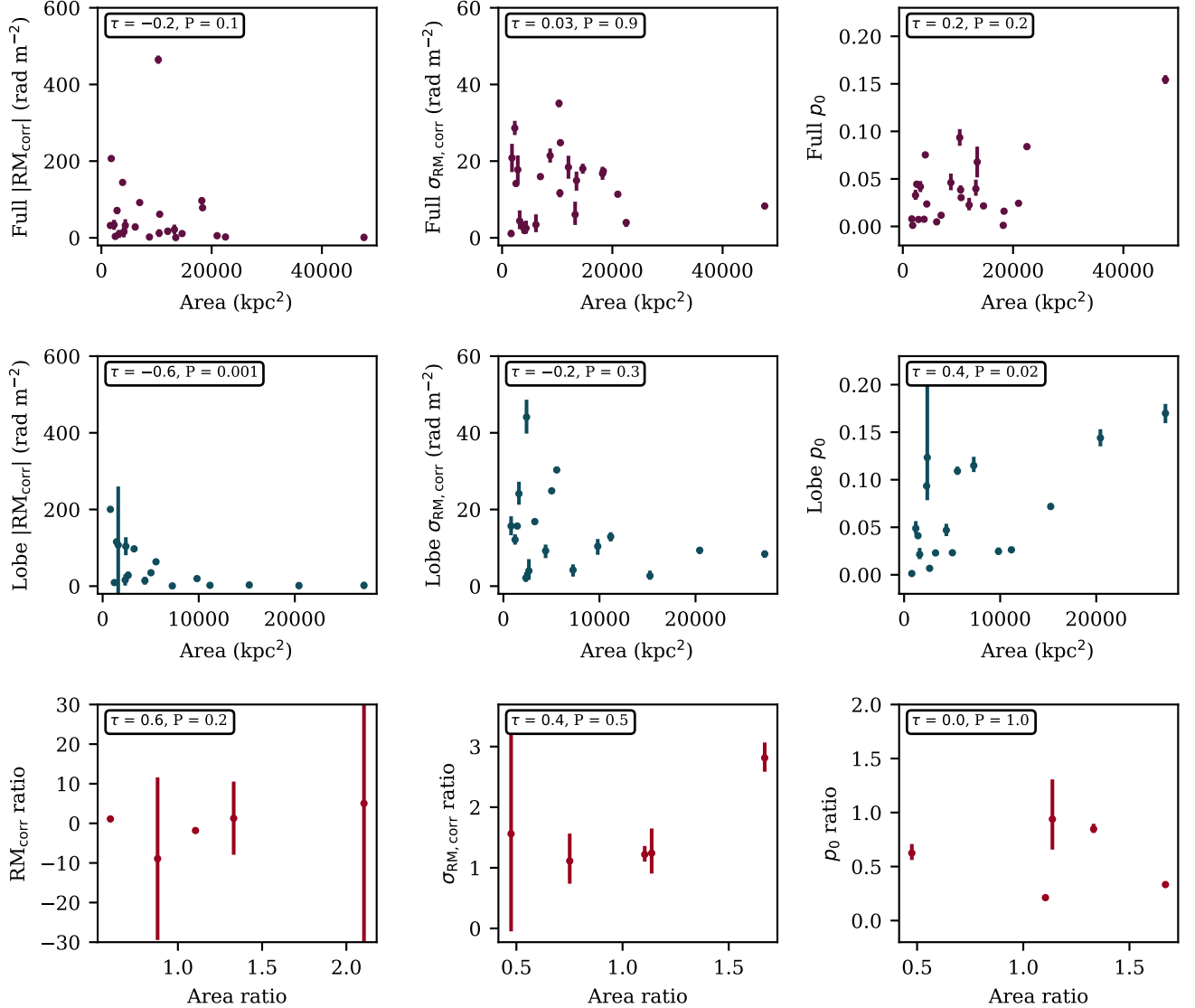


Figure 7. Model parameters versus total integrated physical area for the full-source integrated spectra (top row), the individual lobe-integrated spectra (middle row), and the lobe ratios (bottom row). In each panel, the Kendall's tau correlation coefficient, τ , and corresponding P-value for the data is given in the top left corner.

Barkus et al. 2022). To define the direction of bending of our sources, we initially tried using the Python package FILFINDER (Koch & Rosolowsky 2015), however we found that the complicated morphology of many of our sources made it difficult to automate the ridgeline identification process. In addition, not all of the ridgelines were identified by the package in the more complicated sources.

Instead, to identify the ridgelines, we take the derivative of the total intensity image of each source and manually define the ridgelines using the path of the minimum in the gradient image as a guide. We provide plots of the ridgelines for each of our 24 polarized radio

galaxies in Figure 12 in Appendix A. Weżgowiec et al. (2024) perform a similar analysis using a filter to highlight intensity gradients in the image of their source. Some sources require diverging ridgelines instead of a single line running along the entire source (e.g., source J005602 – 012003 of Figure 12 in Appendix A). In all cases, the gradient images show a clear path of the minimum derivative along the source, making identification of a ridgeline straightforward.

We calculate the difference between each independent magnetic field vector (using the random selection processes described above to exclude correlated magnetic field vectors within the same synthesized beam area)

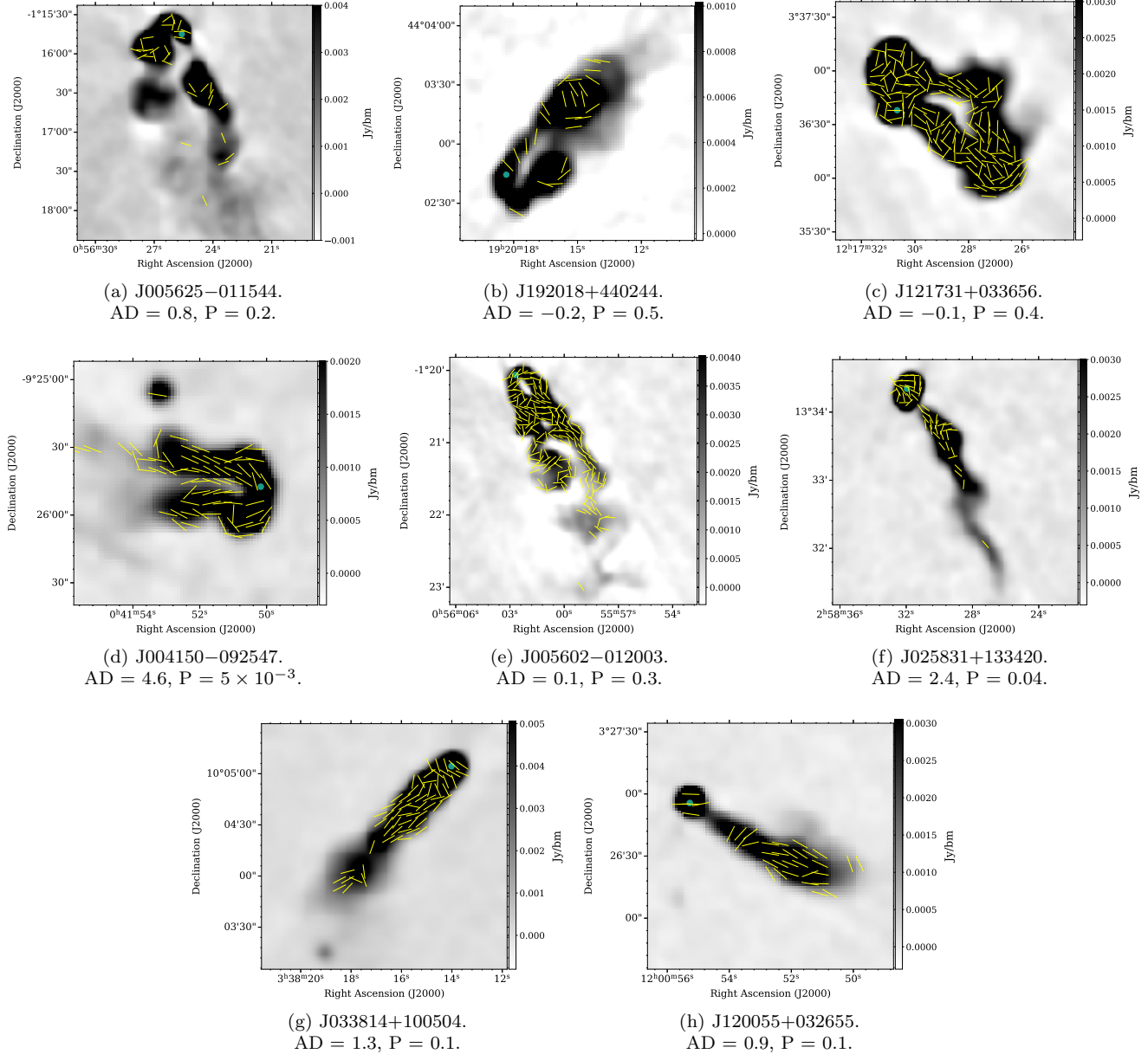


Figure 8. Magnetic field vector maps of the 8 sources with greater than 50 independent vectors. We note that this figure includes the oversampled magnetic field vectors instead of the re-sampled independent field vectors to provide a clearer visualization. The position of the host galaxy in each image is indicated by a cyan circle.

and the slope of the nearest point on the ridgeline. The results are shown in Figure 9.

The distribution of the data in Figure 9 is skewed to smaller angle differences, indicating that the direction of the magnetic field vectors has a preference for alignment with the direction of bending along the sources. The mean and median of the data is $40^\circ.4$ and $36^\circ.8$, respectively, while the mean and median of the randomly drawn distribution is $45^\circ.0$ and $45^\circ.7$, respectively. We draw 1000 random samples and calculate the standard deviation of the means and medians of each distribution

(~ 0.77 and ~ 1.5 , respectively) and find a 6σ significance level, supporting the conclusion that magnetic field vectors preferentially align with the jet bending direction. We discuss the implications of this result in Section 5.2. Because of the generally small number of independent magnetic field vectors in our sources, our ability to assess alignment in the sources individually is limited. A larger sample with an overall higher S/N_{pol} is needed to further investigate alignment with direction of bending. However, as shown by Osinga et al. (2022), sources in galaxy clusters see increased depolarization depending

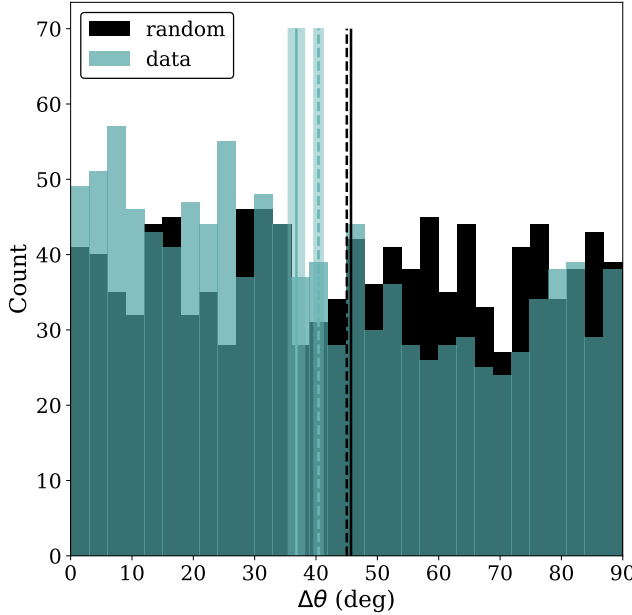


Figure 9. Distribution of the difference in angle, $\Delta\theta$, between the intrinsic magnetic field vectors and the slope of the nearest point on the source ridgeline for each of the 24 radio galaxies in our sample (blue), compared to a randomly generated distribution of angle differences (black). The random distribution is approximately uniform, with a mean (dashed black line) and median (solid black line) of 45.0° and 45.7° , respectively. The observed distribution is skewed toward smaller angular differences, with a mean (dashed blue line) and median (solid blue line) of 40.4° and 36.8° , respectively. Shaded bands around the blue lines indicate the 1σ uncertainty levels, calculated from 1000 realizations of the random distribution.

on their location within the cluster. As a result, building such a sample will require considerably deeper data to recover polarized emission across more sources and over more extended regions within each source (e.g., [Loi et al. 2025](#)).

Although outside the aim of this work, an interesting avenue for future investigation would be to compare direction of bending direction with the location of the brightest cluster galaxy in each cluster, as has been done in previous studies of bent radio galaxy trajectories (e.g., [Sakelliou & Merrifield 2000](#); [Golden-Marx et al. 2021](#)). The availability of magnetic field vector information in our sample could provide valuable additional insight into such analyses.

4.6. RM and derotated polarization angle gradient alignment

To test whether the RM observed across our bent radio galaxies originates local to the source or is dominated by foreground contributions, we analyze the align-

ment between the spatial gradients of the RM and of the intrinsic polarization angle, ψ_0 , maps for each of our sources. A correlation between the gradients of these two quantities may indicate a shared physical origin.

We follow the approach outlined by [Ensslin et al. \(2003\)](#), which builds upon work by [Rudnick & Blundell \(2003\)](#). [Ensslin et al. \(2003\)](#) introduced the gradient alignment statistic (GAS), which compares the spatial gradients of RM and of ψ_0 to test for alignment while correcting for noise-related biases. The alignment statistic, A , is defined as:

$$A[\mathbf{p}, \mathbf{q}] = \frac{\int d^2x \langle \mathbf{p}(\mathbf{x}), \mathbf{q}(\mathbf{x}) \rangle}{\int d^2x |\mathbf{p}(\mathbf{x})| |\mathbf{q}(\mathbf{x})|}, \quad (3)$$

where $\mathbf{p}(\mathbf{x}) = \nabla \text{RM}$ and $\mathbf{q}(\mathbf{x}) = \nabla \psi_0$ ³, and $\langle \mathbf{p}(\mathbf{x}), \mathbf{q}(\mathbf{x}) \rangle$ is defined as:

$$\langle \mathbf{p}(\mathbf{x}), \mathbf{q}(\mathbf{x}) \rangle = \frac{(p_x^2 - p_y^2)(q_x^2 - q_y^2) + 4p_x p_y q_x q_y}{\sqrt{p_x^2 + p_y^2} \sqrt{q_x^2 + q_y^2}}. \quad (4)$$

A measures the correlation in gradient directions between RM and ψ_0 , and will have a value of 0 for uncorrelated maps and a value of 1 for full correlated maps. The gradient vector product statistic, V , is defined as:

$$V[\mathbf{p}, \mathbf{q}] = \frac{\int d^2x \mathbf{p}(\mathbf{x}) \cdot \mathbf{q}(\mathbf{x})}{\int d^2x |\mathbf{p}(\mathbf{x})| |\mathbf{q}(\mathbf{x})|}, \quad (5)$$

and accounts for spurious alignment due to correlated noise. The sum $A + V$ provides a noise-corrected measure of alignment between the gradients, with increasing values indicating stronger structural correspondence between RM and ψ_0 .

We compute A , V , and $A + V$ for 22 of the 24 polarized radio galaxies in our sample (two of our 24 sources are excluded due to an insufficient number of polarized pixels with which to calculate a gradient). As in Sections 4.4 and 4.5, we only use pixels within the 10σ total intensity contour with $\text{S/N}_{\text{pol}} > 6$ to calculate the statistics. A histogram of the resulting $A + V$ values is shown in Figure 10. The distribution has a mean value of -0.03 and a standard deviation of 0.29 .

Of the 22 sources, 19 have $A + V < 0.2$, consistent with no structural alignment between RM and ψ_0 and indicating that the origin of the observed RMs across these sources is foreground to the source. While there is no strict threshold distinguishing co-aligned from unaligned sources, a value of ~ 0.3 is consistent with the interpretation of [Ensslin et al. \(2003\)](#) that such sources

³ The gradient of ψ_0 is calculated using subtraction modulo 180° to account for the cyclic nature of the parameter.

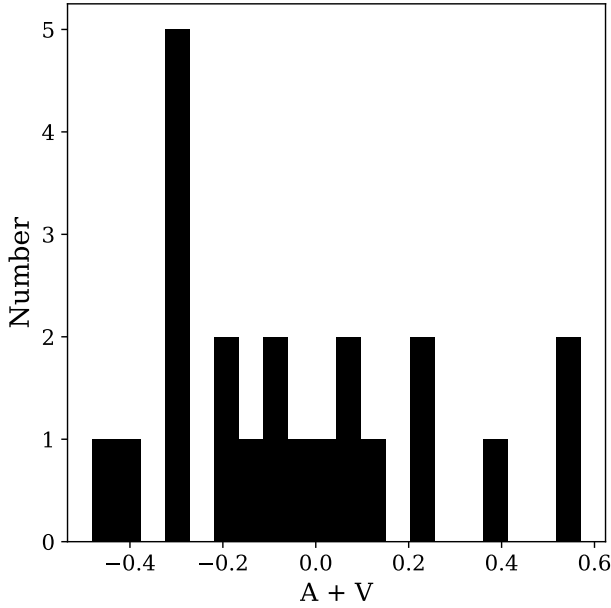


Figure 10. Distribution of the $A + V$ alignment statistic for 22 of the 24 radio galaxies in our sample.

exhibit little to no magnetic field alignment. The remaining 3 sources have $A + V > 0.3$, which we interpret as indicating co-alignment and which suggests that the origin of the observed RMs is local or intrinsic to these sources. We discuss these results in more detail in Section 5.3.

5. DISCUSSION

In this section, we first interpret our key observational results, then consider the implications for RM grid experiments, and finally discuss expectations for future wide-field polarization surveys.

5.1. Lack of Correlation Between Polarization Parameters and Bending Angle

We find no statistically significant correlation between bending angle and either σ_{RM} or $|\text{RM}|$ in our sample of polarized bent radio galaxies. This result is somewhat surprising in light of previous work by Osinga et al. (2022, 2025) and van der Jagt et al. (2025), who find correlations between RM and bending angle and R/R_{500} (see Section 4.1). These studies imply that both polarization properties and radio galaxy morphology are sensitive to the ICM environment, either locally or integrated along the line of sight, and might be expected to correlate with each other. However, in our sample, neither σ_{RM} nor $|\text{RM}|$ show a statistically significant correlation with bending angle (see Figure 4).

Two broad interpretations can account for this result: (1) a correlation may exist but remains undetectable

given the resolution of our observations or the size of our sample, or (2) there is no intrinsic correlation between bending angle and these polarization parameters. The first explanation is supported by our correlation statistics. In Section 4.1, we showed that although Osinga et al. (2025) (a sample of ~ 800 polarized components) and van der Jagt et al. (2025) (a sample of 109 bent radio galaxies) report significant correlations between RM, bending angle, and R/R_{500} , our data reveal only weak, statistically insignificant relationships among these parameters. The weakened correlations between RM and position in the cluster in our sample may therefore explain the lack of correlation between RM and bending angle. To test this explicitly, we drew 1000 random subsamples of 24 sources from the Osinga et al. (2025) and van der Jagt et al. (2025) samples individually. For the Osinga et al. (2025) sample, we selected only components located inside the cluster. The full sample shows a strong correlation between $|\text{RM}|$ and R/R_{500} ($\tau = -0.4$, $p = 8 \times 10^{-24}$), but the 1000 random subsamples typically yielded weaker results (median $p = 0.01$, mean $p = 0.1$, with standard deviation $p = 0.1$). We note, however, that Osinga et al. (2025) measures RMs of individual components rather than integrated spectra, in contrast to our approach, making direct comparison with our results more difficult. Similarly, the van der Jagt et al. (2025) sample shows a correlation between bending angle and R/R_{500} in the full dataset ($\tau = -0.3$, $p = 6 \times 10^{-5}$), while the 1000 random subsamples of 24 sources also yielded weaker correlation results (median $p = 0.1$, mean $p = 0.2$, with a standard deviation $p = 0.2$). These results demonstrate that when restricted to small samples, the correlations reported in larger studies can weaken substantially, consistent with the lack of correlation we observe.

Alternatively, the lack of correlation may be understood in terms of the distinct spatial scales and physical quantities that these observables probe. The ICM is expected to be turbulent across a broad range of scales in both merging and relaxed clusters (Subramanian et al. 2006; Dolag et al. 2008; Vazza et al. 2012). RM and σ_{RM} reflect integrated properties of the magnetized plasma along the entire line of sight, such as total electron column density and fluctuations in the line-of-sight magnetic field. Bending angle, by contrast, is governed by ram pressure (Jones & Owen 1979; Vallee et al. 1981; Garon et al. 2019), $P_{\text{ram}} \propto \rho_{\text{ICM}} v^2$, which depends on the local ICM density (ρ_{ICM}) and the galaxy's velocity relative to the ICM (v). As such, it reflects local conditions at the galaxy's position within the cluster. If two bent radio galaxies have the same bending angle and are located at the same projected distance from the cluster

center, but one lies on the near side of the cluster and the other on the far side, their measured RMs may differ significantly due to the depth and structure of the intervening ICM. Similarly, turbulence in the ICM introduces local fluctuations in density, potentially leading to spatial and temporal variations in the ram pressure experienced by the jet (e.g., [Tonnesen & Bryan 2008](#)). These differences in how RM, σ_{RM} , and bending angle probe the cluster environment could obscure any direct relationship between them.

Projection effects further complicate the interpretation of any potential correlation. We observe bending angle only as projected in the sky plane. A galaxy moving with a significant line-of-sight velocity through a dense region of the ICM will experience strong ram pressure and enhanced RM at its leading edges as magnetic field lines become compressed ([Pfrommer & Dursi 2010](#)), but its projected bending may appear small due to its projection onto the 2D plane. Conversely, the same galaxy moving largely in the plane of the sky will exhibit its full bending. Thus, even if two galaxies experience comparable physical ram pressure, their observed bending angles may differ substantially depending on orientation. Similarly, RM and σ_{RM} are affected by the galaxy's depth in the cluster and the structure of the ICM along the line of sight, introducing additional scatter between galaxies at similar projected radii.

In addition, differences in sample selection may contribute to the absence of correlation. [van der Jagt et al. \(2025\)](#) select their sample in total intensity, while our sample is selected based on detected polarization. This difference in selection could introduce a bias in RM properties. Polarized sources are more easily detected when Faraday depolarization is low, which may favor sources located on the near side of the cluster or along less dense, less turbulent sightlines. As a result, our polarization-selected sample may underrepresent the full range of RM values observed near the cluster center. If so, this would further limit the dynamic range in RM and could weaken any potential correlation with bending angle. However, low polarization can also result from intrinsic source properties, which may limit the extent to which Faraday effects alone account for the observed detection bias.

Jet bending is a time-dependent process, reflecting the dynamical evolution of radio galaxies as they move through the ICM. Simulations by [O'Neill et al. \(2019\)](#) show that a NAT morphology evolves through an earlier WAT morphology, supporting the idea that bending angle increases with time. While [Morsony et al. \(2013\)](#) demonstrate that the bending angle (or radius of curvature) is primarily determined by environmental and jet

properties—such as jet luminosity, jet velocity, AGN velocity, and ICM density—they also find that the radius of curvature can vary by up to 25 percent for fixed input parameters. Moreover, they show that the length of the radio tail trailing the galaxy grows over time, consistent with an extended emission history. These results suggest that although bending angle is largely determined by environmental and jet properties, morphological features may evolve over time, which could weaken any observed correlation with turbulent quantities like σ_{RM} in a statistical sample.

Finally, we note that σ_{RM} may be more strongly correlated with ICM turbulence that varies systematically with position in the cluster, rather than with bending angle. We perform a Kendall's τ correlation test between σ_{RM} and R/R_{500} in the lobe spectra and find $\tau = -0.7$ and $P = 5 \times 10^{-4}$. This does not meet our threshold for a potential correlation, but it does indicate a possible dependence between these two parameters. This suggests that σ_{RM} is correlated with the position of a radio galaxy within the cluster, and that we may be tracing turbulence from the intervening ICM, which is largely dependent on the distance from the cluster center and not bending angle. This agrees with cluster magnetism studies that use resolved radio galaxies as probes of the ICM (e.g., [Bonafede et al. 2010](#)).

In summary, we find no statistically significant correlation between σ_{RM} and bending angle in our sample of bent radio galaxies. This result may reflect a genuine lack of connection between radio galaxy morphology and small-scale turbulence in the ICM. While our data are consistent with a scenario in which σ_{RM} traces turbulence along the line-of-sight and where bending angle reflects local dynamical conditions or time-evolution, a more robust examination of any potential correlation will require larger samples and higher-resolution observations.

5.2. Magnetic field vector coherence and alignment with direction of bending

In Figure 8 we showed that magnetic field vector coherence is present in many of our more polarized sources, and Figure 9 hints at a preference for magnetic field vectors to align with the direction of bending, or fluid flow. This implies that the bending or distortion of radio galaxies from a linear morphology does not disorder the large-scale magnetic field within the source jets and lobes. [O'Neill et al. \(2019\)](#) conducted the first high-resolution 3D magnetohydrodynamic simulation focusing on the evolution of a bipolar-jet radio galaxy interacting with a constant crosswind. The authors found that the jets generally remain coherent during and after

the bending process, although if instabilities arise they can disrupt the jets. O’Neill et al. (2019) also found that the stress from the jet-bending process can convert the initial toroidal magnetic field into a predominantly poloidal configuration. Helical magnetic fields are also thought to be present in the jets of radio galaxies, which can manifest (among many other ways) as an orthogonal polarization pattern along the jet of a galaxy (Gabuzda 2018). If helical magnetic fields are present in some of the sources and multiple periods of the helical path are averaged within the synthesized beam, this could potentially obscure any relationship between magnetic field vector orientation and direction of bending.

To our knowledge, there are few examples of magnetic field vector maps of well resolved bent radio galaxies. In a map of the asymmetric radio galaxy 4C 70.19 (believed to be a member of a galaxy group and not a galaxy cluster) from Weżgowiec et al. (2024), the magnetic field vectors show a high level of coherence with regions where the vectors are generally aligned with the direction of fluid flow as well as region where the vectors appear nearly perpendicular to the direction of flow. Together these previous studies suggest that alignment or anti-alignment with the direction of bending may be dependent on which part of the source we are probing (e.g., jet or lobe, inner lobe or the edges). Many of our sources are depolarized across much of the source. In each of our 8 sources with well-sampled magnetic field vectors, we may be probing the magnetic field vectors in different regions of the source (e.g., inner jet versus outer jet versus lobe).

The results of our magnetic field vector analysis are highly dependent on resolution and angular size of the source. Lower resolution combined with small angular size will average more magnetic field vectors together within the synthesized beam. We are also limited by S/N, which limits the number of pixels with a reliably measured magnetic field vector. The majority of our sources have few magnetic field vectors with which to test coherence and alignment (see Section 4.4). A larger sample of sources with higher S/N_{pol} and better-resolved spatial structure would be ideal for future analysis.

5.3. Implications of RM- ψ_0 gradient alignment analysis

The gradient alignment analysis in Section 4.6 indicates that the Faraday rotation in most of our bent radio galaxies is dominated by foreground material. Of the 22 sources examined, 19 have $A + V \lesssim 0.3$, pointing to no significant physical correlation between RM and ψ_0 and therefore to a foreground RM origin. Only 3 sources reach $A + V > 0.3$, suggestive of a local RM origin. The

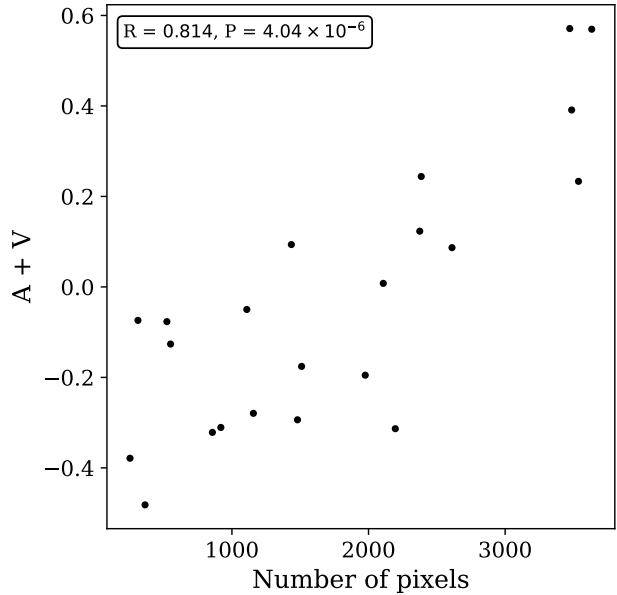


Figure 11. $A + V$ alignment statistic versus the number of pixels used in the calculation of the statistic. A statistically significant correlation is detected between the two quantities.

distribution of $A + V$ values is reasonably narrow and centered on zero ($\mu = -0.03$ and $\sigma = 0.29$), reinforcing the view that large-scale RM- ψ_0 alignment is generally absent in our sample. These findings are similar to those of Ensslin et al. (2003), who reported $A + V < 0.2$ for cluster-member radio galaxies PKS 1246–410, Cygnus A, Hydra A, and 3C 465.

Figure 11 plots $A + V$ against the number of polarized pixels present in each of the source gradient maps. Pixel count serves as a proxy for how finely a source is sampled in polarized intensity: a larger tally of pixels above $S/N_{pol} > 6$ means more independent measurements of RM and ψ_0 across the lobes. However, pixel count also depends on the resolution and angular size, so this is not a perfect proxy. A Pearson correlation test identifies a statistically significant relationship between $A + V$ and pixel count ($R = 0.814$, $P = 4.04 \times 10^{-6}$). This indicates that the apparent presence (or absence) of RM- ψ_0 gradient co-alignment may be sensitive to both resolution and polarized S/N. The dependence of the $A + V$ statistic on number of pixels comes from the V term, which shows the same dependence on pixel count as the sum, while the A term shows no dependence.

Our gradient alignment results are consistent with the lack of a statistically significant correlation between RM and bending angle seen in Section 5.1, which indicates that we are primarily probing foreground ICM properties rather than source properties. This supports the interpretation that bent radio galaxies are not a biased

population in terms of Faraday depth and can be reliably used to probe the magnetized ICM. However, we note that this conclusion may be affected by the dependence of the $A + V$ statistic on pixel count, and we therefore caution against overinterpreting its results. A larger, more uniformly sampled set of bent radio galaxies will be essential to confirm these findings and to better isolate observational biases from genuine differences in Faraday rotation origin.

Overall, our results lead to the conclusion that we are likely primarily probing large-scale ICM effects that are not dependent on bending angle. This is consistent with the findings of Osinga et al. (2022), who show that radio galaxies embedded in a cluster show similar depolarization profiles to radio galaxies that are background to the cluster. This implies that local ICM effects are not dominant in statistical samples.

6. BENT RADIO GALAXIES AS A POPULATION OF RM GRID SOURCES

Maps of RMs on the sky, known as RM grids (Gaensler et al. 2004), are an invaluable method of probing magnetic field geometry in many different environments, including the large-scale Galactic magnetic field (Mao et al. 2010; Van Eck et al. 2011; Hutschenreuter et al. 2022), molecular clouds (Tahani et al. 2018), the jets and lobes of radio galaxies (Feain et al. 2009; O’Sullivan et al. 2018), galaxy clusters (Bonafede et al. 2010; Anderson et al. 2021), and the cosmic web (Vernstrom et al. 2019; Amaral et al. 2021; Carretti et al. 2022). Current surveys such as the Polarisation Sky Survey of the Universe’s Magnetism (POSSUM; Gaensler et al. 2025), as well as the upcoming Square Kilometre Array, will greatly increase the number of polarized source detections that can be used in RM grid experiments (Johnston-Hollitt et al. 2015b).

Since bent radio galaxies typically reside in overdense environments like galaxy clusters and groups, they will be a subset of the population of sources used to probe the magnetic field strength and geometry in clusters. While Osinga et al. (2025) find a correlation between RM scatter and projected distance to the cluster center, and van der Jagt et al. (2025) find a correlation between bending angle and projected distance to cluster center, our work shows no correlation between RM and bending angle at the physical resolutions of our data (synthesized beam extends of 3–46 kpc, with mean and median values 18.8 and 18.4 kpc, respectively). This lack of statistically significant correlation between bending angle and RM is evidence that we are probing foreground ICM effects, and that bent radio galaxies are likely not bias-

ing the RM-distance correlation. Therefore, bent radio galaxies at the typical resolution of this study are likely a useful population of sources for probing ICM magnetic field properties with RM grid studies of galaxy clusters.

6.1. Estimated bent radio galaxy sample from POSSUM

As noted above, a larger statistical sample size would provide a more robust determination of the presence or absence of correlation between bending angle and polarization properties of a source. POSSUM is currently surveying 20 000 deg² of the sky at Declination (J2000) $< 0^\circ$ with the Australian Square Kilometre Array Pathfinder (ASKAP; Hotan et al. 2021). Here we estimate the number of bent radio galaxies that will be present in the full POSSUM survey catalogue.

The all-sky Planck catalogue of Sunyaev-Zeldovich sources (PSZ2; Planck Collaboration et al. 2016) contains 818 galaxy cluster detections at Declination $< 0^\circ$. Of these 818 clusters, 499 are previously optically-identified clusters with known redshifts, and of this subset, 348 (70%) are at a redshift of $z \leq 0.3$, where 0.3 is approximately the highest redshift in our sample. We find that the 24 polarized sources in our sample are distributed across 19 clusters from the 124 observed by Osinga et al. (2022) (see Section 2). However, the POSSUM synthesized beam width will be 20 arcsec, which is $\sim 2\text{--}3 \times$ larger than the beam widths in our sample. Of the 24 polarized sources, 16 would be resolved enough in the POSSUM survey to still have at least 3 synthesized beam widths across the source. These 16 sources are found in 15 galaxy clusters, corresponding to 12% of the total number of clusters originally observed ($\frac{15}{124}$), and 1.1 polarized galaxies per cluster.

From these calculations, we estimate that the POSSUM survey catalogue will contain 348 PSZ2 clusters $\times 0.12 \times 1.1$ polarized bent radio galaxies per cluster, which is 46 bent galaxies with a range of bending angles. We include the caveat that the mass distribution of clusters in the full PSZ2 survey will not match that of our sample, and is likely to extend to lower-mass systems. While the occurrence of WATs and NATs as a function of cluster mass is not well constrained, bent radio galaxies are known to be preferentially associated with over-dense environments. They have, however, also been detected in lower-mass groups in both observations (e.g., Freeland et al. 2008) and simulations (e.g., Morsony et al. 2013), indicating that bending can occur across a range of environments. Nonetheless, if bent sources are more common in higher-density systems, it is plausible that lower-mass clusters will host fewer tailed radio galaxies, making our estimate an upper limit. However,

additional polarized bent radio galaxies can likely be added to the sample once redshifts are measured for the new PSZ cluster detections. If the redshift distribution is similar in the newly discovered galaxy clusters (which is not necessarily expected), we could expect up to an additional 30 bent radio galaxies. As well, all galaxy clusters in the POSSUM survey area should be inspected. Any galaxies with a larger angular extent (at least 3 synthesized beam widths across the source) in higher redshift ($z > 0.3$) clusters that also meet our sample selection criteria should be included in the sample.

If we instead consider the Spectrum-Roentgen Gamma mission with the extended ROentgen Survey with an Imaging Telescope Array (SRG/eROSITA; Sunyaev et al. 2021; Predehl et al. 2021) catalogue (Bulbul et al. 2024), we estimate a significantly larger sample. SRG/eROSITA surveyed $\sim 20\,000$ deg 2 of the sky at X-ray frequencies. Only regions of the survey that overlapped with the DESI Legacy Survey Data Releases 9 and 10 (for optical follow-up of cluster detections) and that did not contain high Galactic-latitude supernova remnants were used, leaving a final survey area for cluster detection of $13\,116$ deg 2 . The catalogue contains 10 248 galaxy clusters with redshift at declination $< 0^\circ$, the majority of which are new detections (Bulbul et al. 2024). Bulbul et al. (2024) construct a more robust, securely confirmed catalogue of 5259 galaxy clusters, which we here use to estimate sample size in the POSSUM survey. Of the 5259 securely confirmed cluster detections, 2337 are at declination $< 0^\circ$ and are at a redshift of $z \leq 0.3$. Using the same polarized source density per cluster and percentage of cluster with polarized sources that meet our selection requirements as above, we estimate a sample of polarized bent radio galaxies in POSSUM of at least $2337 \times 0.12 \times 1.1 = 308$ bent radio galaxies. This number may be even larger, since the SRG/eROSITA survey does not cover the entire sky at declination $< 0^\circ$, and because we are only considering the smaller catalogue of securely confirmed cluster detections. Similar to the caveat described for the PSZ2 clusters, the mass distribution of the eROSITA clusters is not expected to match that of our sample, so our estimates here should likewise be considered an upper limit.

6.2. Estimated bent radio galaxy sample from the SKA

The forthcoming all-sky survey with the Square Kilometre Array, particularly SKA1-Mid Band 2⁴ (SKA1-Mid2), will deliver major improvements in both angular

resolution and sensitivity over existing wide-area radio surveys. SKA1-Mid2 is expected to observe $\sim 30\,000$ deg 2 of the sky over 950–1760 MHz with a resolution of approximately 2 arcsec and a sensitivity of 4 μ Jy/beam (Heald et al. 2020), representing an order-of-magnitude improvement over the POSSUM survey in both respects.

These enhancements are expected to significantly increase the number of bent radio galaxies that meet the selection criteria for studies such as this one. In our current dataset, we find an average of 1.1 polarized radio galaxies per cluster that are sufficiently resolved (see Section 6.1) and meet our S/Npol threshold. The five-fold improvement in sensitivity between POSSUM (~ 20 μ Jy/beam) and SKA1-Mid2 (4 μ Jy/beam) implies a larger number of detectable sources. Using the cumulative number count distribution for polarized sources, which scales approximately as $P_{det}^{-0.6}$ (Rudnick & Owen 2014), where P_{det} is the detection limit in polarization, we estimate that SKA1-Mid2 will detect approximately three times as many polarized radio galaxies per cluster as POSSUM, based on sensitivity alone. Updating our estimates from Section 6.1, we estimate that SKA1-Mid2 will be able to detect $3.3 \times 308 = 1016$ polarized radio galaxies at $z \leq 0.3$ and declination < 0 with the SRG/eROSITA catalogue.

If we remove the redshift constraint, SRG/eROSITA has 4516 securely detected clusters out to $z \sim 0.8$, nearly double the number present at $z \leq 0.3$. Given its sensitivity, we expect SKA1-Mid2 to detect polarized radio galaxies in all of these clusters (e.g. Johnston-Hollitt et al. 2015a). Additionally, the order-of-magnitude improvement in angular resolution from POSSUM (21 arcsec) to SKA1-Mid2 (2 arcsec) will further increase the number of sources that satisfy our ≥ 3 -beamwidth selection criterion.

Higher angular resolution will also enable improved mapping of the intrinsic magnetic field vectors within individual sources. In Section 4.5, we report a statistically significant preference for alignment between magnetic field vectors and the direction of jet bending. However, this preference for alignment may be underestimated due to beam-averaging of sharp angle changes (e.g., a change in direction of jet-bending) or helical magnetic field structures. The increased resolution and sample size provided by SKA1-Mid2 will allow this potential alignment to be tested in a more robust and statistically powerful way.

We compare our results to other bent radio galaxy samples in the literature. We estimate that POSSUM will contain 308 polarized bent radio galaxies (0.015 deg $^{-2}$) and the SKA will contain 1016 polarized bent radio galaxies (0.034 deg $^{-2}$), requiring that sources are

⁴ <https://www.skao.int/en/science-users/118/ska-telescope-specifications>

extended by at least three beamwidths, are polarized, and lie at $z \leq 0.3$. In contrast, Wing & Blanton (2011) identified 272 bent and 449 straight radio galaxies through an automated search in total intensity in the VLA Faint Images of the Radio Sky at Twenty Centimeters (FIRST; Becker et al. 1995) survey over ~ 9000 deg 2 . They also identified an additional 166 bent radio galaxies through a visual search over a ~ 3000 deg 2 region of the same survey, giving a total average sky density of 0.068 deg $^{-2}$. Similarly, Paterno-Mahler et al. (2017) reported 646 bent radio galaxies in total intensity in the high-redshift Clusters Occupied by Bent Radio AGN (COBRA) Survey survey (a sky density of 0.072 deg $^{-2}$), while Vardoulaki et al. (2025) found 19 bent radio galaxies in total intensity in the 2 deg 2 extragalactic COSMOS field (a sky density of 9.5 deg $^{-2}$).

Assuming that only $\sim 20\%$ of extended sources are polarized (we find that 156 of the 704 total extended sources in the Osinga et al. 2022 catalogue show some level of polarization) the Wing & Blanton (2011) and Paterno-Mahler et al. (2017) densities both reduce to 0.014 deg $^{-2}$, broadly consistent with our POSSUM estimate. The COSMOS polarized bent radio galaxy density remains substantially higher, likely due to the subarcsecond resolution of some of the Vardoulaki et al. (2025) observations as well as the absence of a redshift limit. Variations in redshift range (the majority of the Paterno-Mahler et al. 2017 and Vardoulaki et al. 2025 sample is at $z > 0.3$), no requirement of cluster membership, and angular resolution and sensitivity make direct comparison between these samples and ours difficult, but they also indicate that the true sample size of polarized bent radio galaxies in the POSSUM and SKA surveys will be larger than we estimate if our redshift restrictions are relaxed.

7. CONCLUSION AND FUTURE WORK

In this work, we present the first polarization study of a large number (24) of polarized radio galaxies with varying degrees of bending. We test for correlations between bending angle and the polarization properties $|\text{RM}_{\text{corr}}|$, σ_{RM} , and fractional polarization. We find no statistically significant correlation between these properties and bending angle or integrated physical area. We do find a potential correlation between lobe σ_{RM} and bending angle ($P = 6 \times 10^{-4}$), which does not meet our significance threshold. Future larger samples of bent radio galaxies from POSSUM and SKA will be able to perform more robust statistical tests to determine whether this potential correlation is a result of selection effects or a true physical relationship between the parameters.

Overall, our results lead to the conclusion that we are primarily probing large-scale ICM effects, which are not dependent on bending angle, and not the intrinsic polarization properties of the sources.

We find coherence in the polarization angles in 8 of our more highly polarized sources, suggesting that the large-scale magnetic fields are generally organized as a radio galaxy bends. We calculate the difference between the direction of magnetic field vectors and the direction of bending with our sources, and we find that the magnetic field vectors show a preference for alignment with the direction of bending, with a 6σ significance level.

We discuss the use of bent radio galaxies in RM grid studies of galaxy cluster magnetic fields. We conclude that the use of bent radio galaxies at the typical physical resolutions of our sample in the construction of cluster RM grids should not bias values of magnetic field strength estimated from the relation between RM and depolarization and distance to the cluster center. Finally, using galaxy cluster detections from PSZ and SRG/eROSITA, we estimate that the 20 000 deg 2 POSSUM survey area and the anticipated $\sim 30 000$ deg 2 SKA-Mid2 survey will contain $\gtrsim 300$ and $\gtrsim 1000$ polarized radio galaxies, respectively, with a range of bending angles. These estimates assume a similar redshift distribution and number of beamwidths across each source as our sample, and they represent a 1–2 order of magnitude increase over the current dataset.

Further analysis to determine if the origins of the measured RMs are foreground to the galaxies is needed. A larger sample of bent radio galaxies is needed to perform a more robust statistical test of correlation between polarization properties and bending angle, as well as to further investigate the coherence and alignment of magnetic field vectors in these radio galaxies.

ACKNOWLEDGMENTS

We thank Sarah Bradbury for her guidance in the early stages of using and troubleshooting the FILFINDER package. The Dunlap Institute is funded through an endowment established by the David Dunlap family and the University of Toronto. S.V. acknowledges the support of the Natural Sciences and Engineering Research Council of Canada (NSERC) through grant RGPIN-2022-03163, and of the Canada Research Chairs program. The National Radio Astronomy Observatory and Green Bank Observatory are facilities of the U.S. National Science Foundation operated under cooperative agreement by Associated Universities, Inc. We thank the anonymous reviewer for their careful review of the manuscript and their thoughtful feedback.

APPENDIX

A. RIDGELINES

We here show our ridgeline tracing method. In Figure 12 we plot the derivative maps of the total intensity maps of each of the 24 polarized radio galaxies in our sample. As described in Section 4.5, the ridgeline of each source is traced by minimum path along each jet/lobe region.

REFERENCES

Akahori, T., & Ryu, D. 2010, *ApJ*, 723, 476, doi: [10.1088/0004-637X/723/1/476](https://doi.org/10.1088/0004-637X/723/1/476)

Algeri, S., van Dyk, D. A., Conrad, J., & Anderson, B. 2016, *Journal of Instrumentation*, 11, P12010, doi: [10.1088/1748-0221/11/12/P12010](https://doi.org/10.1088/1748-0221/11/12/P12010)

Amaral, A. D., Vernstrom, T., & Gaensler, B. M. 2021, *MNRAS*, 503, 2913, doi: [10.1093/mnras/stab564](https://doi.org/10.1093/mnras/stab564)

Anderson, C. S., Gaensler, B. M., Feain, I. J., & Franzen, T. M. O. 2015, *ApJ*, 815, 49, doi: [10.1088/0004-637X/815/1/49](https://doi.org/10.1088/0004-637X/815/1/49)

Anderson, C. S., Heald, G. H., Eilek, J. A., et al. 2021, *PASA*, 38, e020, doi: [10.1017/pasa.2021.4](https://doi.org/10.1017/pasa.2021.4)

Andrade-Santos, F., Jones, C., Forman, W. R., et al. 2017, *ApJ*, 843, 76, doi: [10.3847/1538-4357/aa7461](https://doi.org/10.3847/1538-4357/aa7461)

Banfield, J. K., Andernach, H., Kapińska, A. D., et al. 2016, *MNRAS*, 460, 2376, doi: [10.1093/mnras/stw1067](https://doi.org/10.1093/mnras/stw1067)

Barkus, B., Croston, J. H., Piotrowska, J., et al. 2022, *MNRAS*, 509, 1, doi: [10.1093/mnras/stab2952](https://doi.org/10.1093/mnras/stab2952)

Becker, R. H., White, R. L., & Helfand, D. J. 1995, *ApJ*, 450, 559, doi: [10.1086/176166](https://doi.org/10.1086/176166)

Begelman, M. C., Rees, M. J., & Blandford, R. D. 1979, *Nature*, 279, 770, doi: [10.1038/279770a0](https://doi.org/10.1038/279770a0)

Bera, S., Pal, S., Sasmal, T. K., & Mondal, S. 2020, *ApJS*, 251, 9, doi: [10.3847/1538-4365/abb367](https://doi.org/10.3847/1538-4365/abb367)

Bera, S., Sasmal, T. K., Patra, D., & Mondal, S. 2022, *ApJS*, 260, 7, doi: [10.3847/1538-4365/ac5cc4](https://doi.org/10.3847/1538-4365/ac5cc4)

Bera, S. K., Sasmal, T. K., Mondal, S., Fang, T., & Chen, X. 2024, *Universe*, 10, 347, doi: [10.3390/universe10090347](https://doi.org/10.3390/universe10090347)

Blanton, E. L., Gregg, M. D., Helfand, D. J., Becker, R. H., & Leighly, K. M. 2001, *AJ*, 121, 2915, doi: [10.1086/321074](https://doi.org/10.1086/321074)

Blanton, E. L., Gregg, M. D., Helfand, D. J., Becker, R. H., & White, R. L. 2000, *ApJ*, 531, 118, doi: [10.1086/308428](https://doi.org/10.1086/308428)

Bonafede, A., Feretti, L., Murgia, M., et al. 2010, *A&A*, 513, A30, doi: [10.1051/0004-6361/200913696](https://doi.org/10.1051/0004-6361/200913696)

Bulbul, E., Liu, A., Kluge, M., et al. 2024, *A&A*, 685, A106, doi: [10.1051/0004-6361/202348264](https://doi.org/10.1051/0004-6361/202348264)

Burn, B. J. 1966, *MNRAS*, 133, 67, doi: [10.1093/mnras/133.1.67](https://doi.org/10.1093/mnras/133.1.67)

Carretti, E., Vacca, V., O’Sullivan, S. P., et al. 2022, *MNRAS*, 512, 945, doi: [10.1093/mnras/stac384](https://doi.org/10.1093/mnras/stac384)

Chambers, K. C., Magnier, E. A., Metcalfe, N., et al. 2019, The Pan-STARRS1 Surveys. <https://arxiv.org/abs/1612.05560>

de Vos, K., Hatch, N. A., Merrifield, M. R., & Mingo, B. 2021, *MNRAS*, 506, L55, doi: [10.1093/mnrasl/slab075](https://doi.org/10.1093/mnrasl/slab075)

Dehghan, S., Johnston-Hollitt, M., Franzen, T. M. O., Norris, R. P., & Miller, N. A. 2014, *AJ*, 148, 75, doi: [10.1088/0004-6256/148/5/75](https://doi.org/10.1088/0004-6256/148/5/75)

Dey, A., Schlegel, D. J., Lang, D., et al. 2019, *AJ*, 157, 168, doi: [10.3847/1538-3881/ab089d](https://doi.org/10.3847/1538-3881/ab089d)

Dolag, K., Bykov, A. M., & Diaferio, A. 2008, *SSRv*, 134, 311, doi: [10.1007/s11214-008-9319-2](https://doi.org/10.1007/s11214-008-9319-2)

Ensslin, T. A., Vogt, C., Clarke, T. E., & Taylor, G. B. 2003, *ApJ*, 597, 870, doi: [10.1086/378631](https://doi.org/10.1086/378631)

Fanaroff, B. L., & Riley, J. M. 1974, *MNRAS*, 167, 31P, doi: [10.1093/mnras/167.1.31P](https://doi.org/10.1093/mnras/167.1.31P)

Feain, I. J., Ekers, R. D., Murphy, T., et al. 2009, *ApJ*, 707, 114, doi: [10.1088/0004-637X/707/1/114](https://doi.org/10.1088/0004-637X/707/1/114)

Freeland, E., Cardoso, R. F., & Wilcots, E. 2008, *ApJ*, 685, 858, doi: [10.1086/591443](https://doi.org/10.1086/591443)

Gabuzda, D. 2018, *Galaxies*, 7, 5, doi: [10.3390/galaxies7010005](https://doi.org/10.3390/galaxies7010005)

Gaensler, B. M., Beck, R., & Feretti, L. 2004, *New Astronomy Reviews*, 48, 1003, doi: [10.1016/j.newar.2004.09.003](https://doi.org/10.1016/j.newar.2004.09.003)

Gaensler, B. M., Heald, G. H., McClure-Griffiths, N. M., et al. 2025, *Publications of the Astronomical Society of Australia*, 1–32, doi: [10.1017/pasa.2025.10031](https://doi.org/10.1017/pasa.2025.10031)

Garon, A. F., Rudnick, L., Wong, O. I., et al. 2019, *AJ*, 157, 126, doi: [10.3847/1538-3881/aaff62](https://doi.org/10.3847/1538-3881/aaff62)

Golden-Marx, E., Blanton, E. L., Paterno-Mahler, R., et al. 2019, *ApJ*, 887, 50, doi: [10.3847/1538-4357/ab5106](https://doi.org/10.3847/1538-4357/ab5106)

—. 2021, *ApJ*, 907, 65, doi: [10.3847/1538-4357/abcd96](https://doi.org/10.3847/1538-4357/abcd96)

Golden-Marx, E., Moravec, E., Shen, L., et al. 2023, *ApJ*, 956, 87, doi: [10.3847/1538-4357/acf46b](https://doi.org/10.3847/1538-4357/acf46b)

Govoni, F., & Feretti, L. 2004, *International Journal of Modern Physics D*, 13, 1549, doi: [10.1142/S0218271804005080](https://doi.org/10.1142/S0218271804005080)

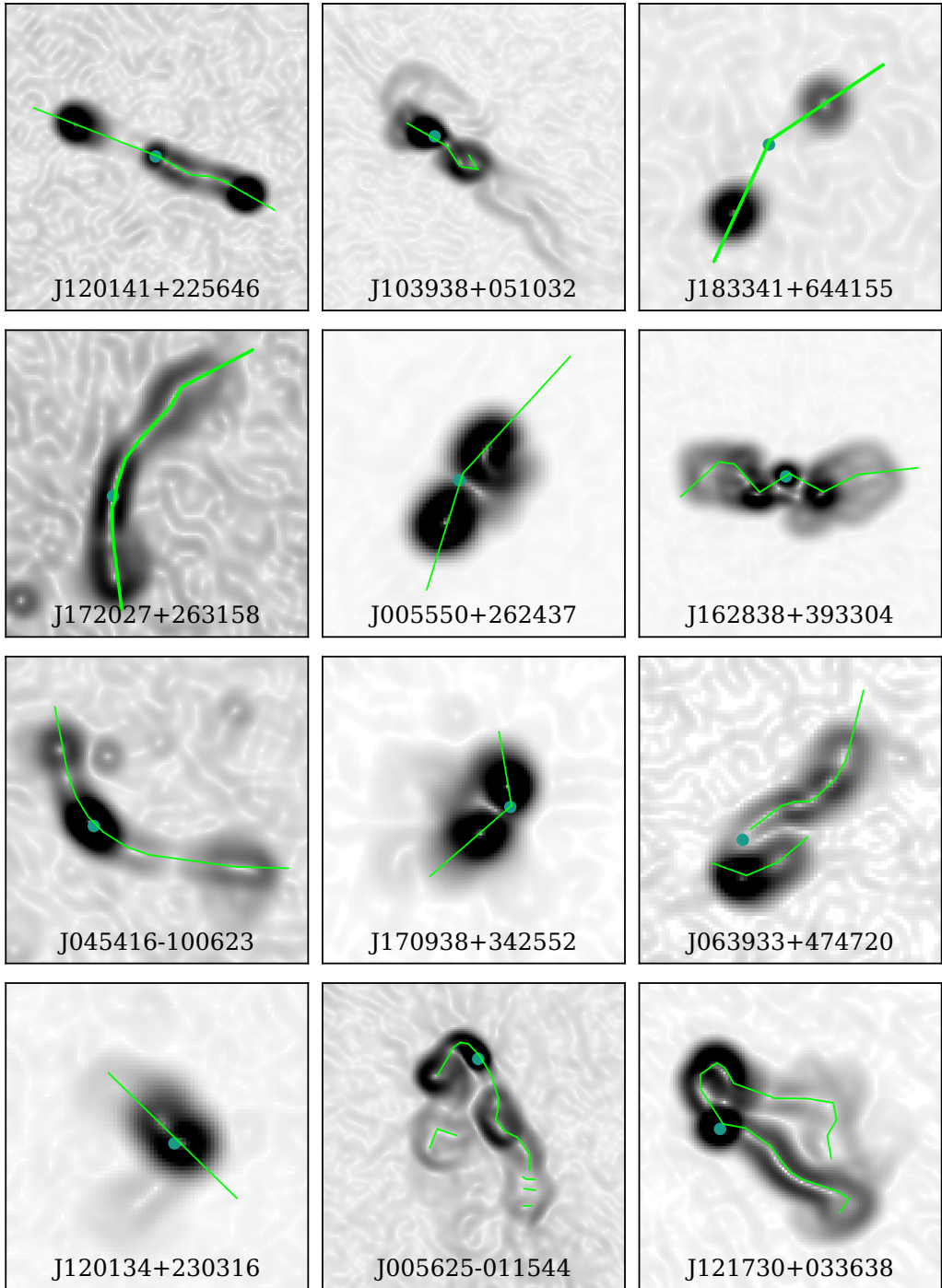


Figure 12. Source ridgelines for the first (ordered by increasing bending angle) 12 polarized radio galaxies in our sample. For each source, the greyscale image is of the derivative of the total intensity MFS image from Figure 2, and the green lines indicate the ridgeline that we have manually traced, following the minimum line along each jet/lobe. The position of the host galaxy in each image is indicated by a cyan circle, and the source identifier is noted at the bottom of each subplot.

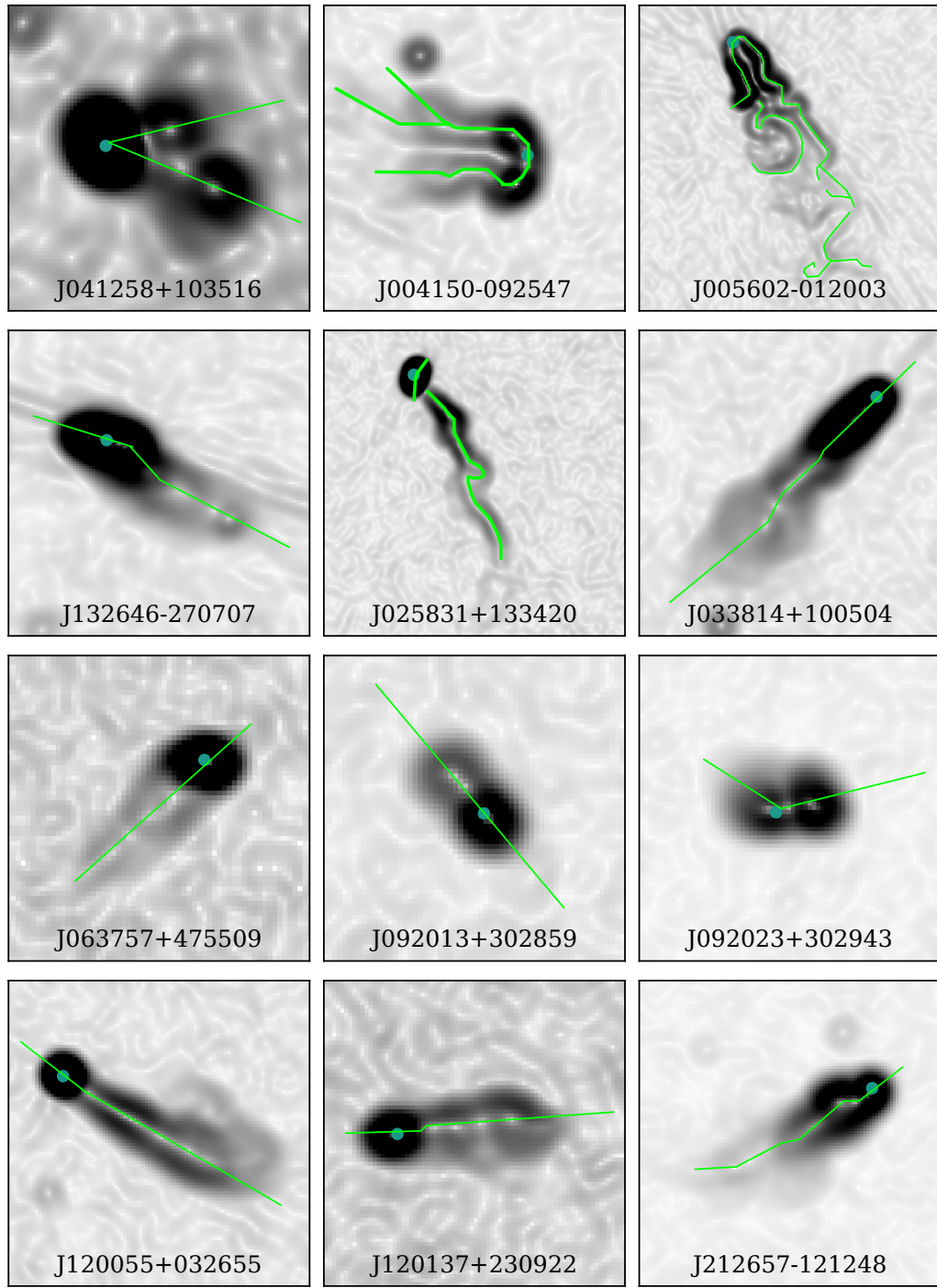


Figure 12. continued. Ridgelines for the remaining 12 polarized radio galaxies in our sample.

Guidetti, D., Laing, R. A., Bridle, A. H., Parma, P., & Gregorini, L. 2011, MNRAS, 413, 2525, doi: [10.1111/j.1365-2966.2011.18321.x](https://doi.org/10.1111/j.1365-2966.2011.18321.x)

Hardcastle, M. J., Sakelliou, I., & Worrall, D. M. 2005, MNRAS, 359, 1007, doi: [10.1111/j.1365-2966.2005.08966.x](https://doi.org/10.1111/j.1365-2966.2005.08966.x)

Heald, G., Mao, S., Vacca, V., et al. 2020, Galaxies, 8, 53, doi: [10.3390/galaxies8030053](https://doi.org/10.3390/galaxies8030053)

Hotan, A. W., Bunton, J. D., Chippendale, A. P., et al. 2021, PASA, 38, e009, doi: [10.1017/pasa.2021.1](https://doi.org/10.1017/pasa.2021.1)

Hutschenreuter, S., Anderson, C. S., Betti, S., et al. 2022, A&A, 657, A43, doi: [10.1051/0004-6361/202140486](https://doi.org/10.1051/0004-6361/202140486)

Jagannathan, P., Bhatnagar, S., Rau, U., & Taylor, A. R. 2017, AJ, 154, 56, doi: [10.3847/1538-3881/aa77f8](https://doi.org/10.3847/1538-3881/aa77f8)

Johnston-Hollitt, M., Dehghan, S., & Pratley, L. 2015a, in Advancing Astrophysics with the Square Kilometre Array (AASKA14), 101, doi: [10.22323/1.215.0101](https://doi.org/10.22323/1.215.0101)

Johnston-Hollitt, M., Govoni, F., Beck, R., et al. 2015b, in Advancing Astrophysics with the Square Kilometre Array (AASKA14), 92, doi: [10.22323/1.215.0092](https://doi.org/10.22323/1.215.0092)

Jones, T. W., & Owen, F. N. 1979, ApJ, 234, 818, doi: [10.1086/157561](https://doi.org/10.1086/157561)

Koch, E. W., & Rosolowsky, E. W. 2015, MNRAS, 452, 3435, doi: [10.1093/mnras/stv1521](https://doi.org/10.1093/mnras/stv1521)

Leahy, J. P. 1987, MNRAS, 226, 433, doi: [10.1093/mnras/226.2.433](https://doi.org/10.1093/mnras/226.2.433)

Loi, F., Serra, P., Murgia, M., et al. 2025, arXiv e-prints, arXiv:2501.05519, doi: [10.48550/arXiv.2501.05519](https://doi.org/10.48550/arXiv.2501.05519)

Ma, Y. K., Mao, S. A., Stil, J., et al. 2019, MNRAS, 487, 3432, doi: [10.1093/mnras/stz1325](https://doi.org/10.1093/mnras/stz1325)

Macquart, J. P., Ekers, R. D., Feain, I., & Johnston-Hollitt, M. 2012, ApJ, 750, 139, doi: [10.1088/0004-637X/750/2/139](https://doi.org/10.1088/0004-637X/750/2/139)

Mahatma, V. H., Hardcastle, M. J., Williams, W. L., et al. 2019, A&A, 622, A13, doi: [10.1051/0004-6361/201833973](https://doi.org/10.1051/0004-6361/201833973)

Mao, S. A., Gaensler, B. M., Havercorn, M., et al. 2010, ApJ, 714, 1170, doi: [10.1088/0004-637X/714/2/1170](https://doi.org/10.1088/0004-637X/714/2/1170)

McMullin, J. P., Waters, B., Schiebel, D., Young, W., & Golap, K. 2007, in Astronomical Society of the Pacific Conference Series, Vol. 376, Astronomical Data Analysis Software and Systems XVI, ed. R. A. Shaw, F. Hill, & D. J. Bell, 127

Mingo, B., Croston, J. H., Hardcastle, M. J., et al. 2019, MNRAS, 488, 2701, doi: [10.1093/mnras/stz1901](https://doi.org/10.1093/mnras/stz1901)

Missaglia, V., Massaro, F., Capetti, A., et al. 2019, A&A, 626, A8, doi: [10.1051/0004-6361/201935058](https://doi.org/10.1051/0004-6361/201935058)

Morris, M. E., Wilcots, E., Hooper, E., & Heinz, S. 2022, AJ, 163, 280, doi: [10.3847/1538-3881/ac66db](https://doi.org/10.3847/1538-3881/ac66db)

Morsony, B. J., Miller, J. J., Heinz, S., et al. 2013, MNRAS, 431, 781, doi: [10.1093/mnras/stt210](https://doi.org/10.1093/mnras/stt210)

Nandi, S., & Saikia, D. J. 2012, Bulletin of the Astronomical Society of India, 40, 121, doi: [10.48550/arXiv.1208.1941](https://doi.org/10.48550/arXiv.1208.1941)

O'Brien, A. N., Norris, R. P., Tothill, N. F. H., & Filipović, M. D. 2018, MNRAS, 481, 5247, doi: [10.1093/mnras/sty2642](https://doi.org/10.1093/mnras/sty2642)

O'Dea, C. P., & Baum, S. A. 2023, Galaxies, 11, 67, doi: [10.3390/galaxies11030067](https://doi.org/10.3390/galaxies11030067)

Offringa, A. R., van de Gronde, J. J., & Roerdink, J. B. T. M. 2012, A&A, 539, A95, doi: [10.1051/0004-6361/201118497](https://doi.org/10.1051/0004-6361/201118497)

O'Neill, B. J., Jones, T. W., Nolting, C., & Mendygral, P. J. 2019, ApJ, 884, 12, doi: [10.3847/1538-4357/ab40b1](https://doi.org/10.3847/1538-4357/ab40b1)

Osinga, E., van Weeren, R. J., Andrade-Santos, F., et al. 2022, A&A, 665, A71, doi: [10.1051/0004-6361/202243526](https://doi.org/10.1051/0004-6361/202243526)

Osinga, E., van Weeren, R. J., Rudnick, L., et al. 2025, A&A, 694, A44, doi: [10.1051/0004-6361/202451885](https://doi.org/10.1051/0004-6361/202451885)

O'Sullivan, S., Brüggen, M., Van Eck, C., et al. 2018, Galaxies, 6, 126, doi: [10.3390/galaxies6040126](https://doi.org/10.3390/galaxies6040126)

O'Sullivan, S. P., Purcell, C. R., Anderson, C. S., et al. 2017, MNRAS, 469, 4034, doi: [10.1093/mnras/stx1133](https://doi.org/10.1093/mnras/stx1133)

O'Sullivan, S. P., Brown, S., Robishaw, T., et al. 2012, MNRAS, 421, 3300, doi: [10.1111/j.1365-2966.2012.20554.x](https://doi.org/10.1111/j.1365-2966.2012.20554.x)

O'Sullivan, S. P., Feain, I. J., McClure-Griffiths, N. M., et al. 2013, ApJ, 764, 162, doi: [10.1088/0004-637X/764/2/162](https://doi.org/10.1088/0004-637X/764/2/162)

O'Sullivan, S. P., Brüggen, M., Vazza, F., et al. 2020, MNRAS, 495, 2607, doi: [10.1093/mnras/staa1395](https://doi.org/10.1093/mnras/staa1395)

Owen, F. N., Burns, J. O., Rudnick, L., & Greisen, E. W. 1979, ApJL, 229, L59, doi: [10.1086/182930](https://doi.org/10.1086/182930)

Owen, F. N., & Rudnick, L. 1976, ApJL, 205, L1, doi: [10.1086/182077](https://doi.org/10.1086/182077)

Pal, S., & Kumari, S. 2023, Journal of Astrophysics and Astronomy, 44, 17, doi: [10.1007/s12036-022-09892-x](https://doi.org/10.1007/s12036-022-09892-x)

Paterno-Mahler, R., Blanton, E. L., Brodwin, M., et al. 2017, ApJ, 844, 78, doi: [10.3847/1538-4357/aa7b89](https://doi.org/10.3847/1538-4357/aa7b89)

Perley, R. A., & Butler, B. J. 2017, ApJS, 230, 7, doi: [10.3847/1538-4365/aa6df9](https://doi.org/10.3847/1538-4365/aa6df9)

Perucho, M., Kovalev, Y. Y., Lobanov, A. P., Hardee, P. E., & Agudo, I. 2012, ApJ, 749, 55, doi: [10.1088/0004-637X/749/1/55](https://doi.org/10.1088/0004-637X/749/1/55)

Pfrommer, C., & Dursi, L. J. 2010, Nature Physics, 6, 520, doi: [10.1038/nphys1657](https://doi.org/10.1038/nphys1657)

Planck Collaboration, Ade, P. A. R., Aghanim, N., et al. 2011, A&A, 536, A8, doi: [10.1051/0004-6361/201116459](https://doi.org/10.1051/0004-6361/201116459)

—. 2015, A&A, 581, A14, doi: [10.1051/0004-6361/201525787](https://doi.org/10.1051/0004-6361/201525787)

—. 2016, A&A, 594, A27, doi: [10.1051/0004-6361/201525823](https://doi.org/10.1051/0004-6361/201525823)

Planck Collaboration, Aghanim, N., Akrami, Y., et al. 2020, *A&A*, 641, A6, doi: [10.1051/0004-6361/201833910](https://doi.org/10.1051/0004-6361/201833910)

Predehl, P., Andritschke, R., Arefiev, V., et al. 2021, *A&A*, 647, A1, doi: [10.1051/0004-6361/202039313](https://doi.org/10.1051/0004-6361/202039313)

Purcell, C. R., Van Eck, C. L., West, J., Sun, X. H., & Gaensler, B. M. 2020, RM-Tools: Rotation measure (RM) synthesis and Stokes QU-fitting, *Astrophysics Source Code Library*, record ascl:2005.003. <http://ascl.net/2005.003>

Rudnick, L., & Blundell, K. M. 2003, *ApJ*, 588, 143, doi: [10.1086/373891](https://doi.org/10.1086/373891)

Rudnick, L., & Owen, F. N. 1976, *ApJL*, 203, L107, doi: [10.1086/182030](https://doi.org/10.1086/182030)

—. 2014, *ApJ*, 785, 45, doi: [10.1088/0004-637X/785/1/45](https://doi.org/10.1088/0004-637X/785/1/45)

Sakelliou, I., & Merrifield, M. R. 2000, *MNRAS*, 311, 649, doi: [10.1046/j.1365-8711.2000.03079.x](https://doi.org/10.1046/j.1365-8711.2000.03079.x)

Sasmal, T. K., Bera, S., & Mondal, S. 2022, *Astronomische Nachrichten*, 343, e20210083, doi: [10.1002/asna.20210083](https://doi.org/10.1002/asna.20210083)

Sebokolodi, M. L. L., Perley, R., Eilek, J., et al. 2020, *ApJ*, 903, 36, doi: [10.3847/1538-4357/abb80e](https://doi.org/10.3847/1538-4357/abb80e)

Sokoloff, D. D., Bykov, A. A., Shukurov, A., et al. 1998, *MNRAS*, 299, 189, doi: [10.1046/j.1365-8711.1998.01782.x](https://doi.org/10.1046/j.1365-8711.1998.01782.x)

Subramanian, K., Shukurov, A., & Haugen, N. E. L. 2006, *MNRAS*, 366, 1437, doi: [10.1111/j.1365-2966.2006.09918.x](https://doi.org/10.1111/j.1365-2966.2006.09918.x)

Sunyaev, R., Arefiev, V., Babushkin, V., et al. 2021, *A&A*, 656, A132, doi: [10.1051/0004-6361/202141179](https://doi.org/10.1051/0004-6361/202141179)

Tahani, M., Plume, R., Brown, J. C., & Kainulainen, J. 2018, *A&A*, 614, A100, doi: [10.1051/0004-6361/201732219](https://doi.org/10.1051/0004-6361/201732219)

Tonnesen, S., & Bryan, G. L. 2008, *ApJL*, 684, L9, doi: [10.1086/592066](https://doi.org/10.1086/592066)

Vallee, J. P., Bridle, A. H., & Wilson, A. S. 1981, *ApJ*, 250, 66, doi: [10.1086/159348](https://doi.org/10.1086/159348)

van der Jagt, S., Osinga, E., van Weeren, R. J., et al. 2025, *arXiv e-prints*, arXiv:2505.17334, doi: [10.48550/arXiv.2505.17334](https://doi.org/10.48550/arXiv.2505.17334)

Van Eck, C. L., Brown, J. C., Stil, J. M., et al. 2011, *ApJ*, 728, 97, doi: [10.1088/0004-637X/728/2/97](https://doi.org/10.1088/0004-637X/728/2/97)

Vardoulaki, E., Vazza, F., Jiménez-Andrade, E. F., et al. 2021, *Galaxies*, 9, 93, doi: [10.3390/galaxies9040093](https://doi.org/10.3390/galaxies9040093)

Vardoulaki, E., Backöfer, V., Finoguenov, A., et al. 2025, *A&A*, 695, A178, doi: [10.1051/0004-6361/202453180](https://doi.org/10.1051/0004-6361/202453180)

Vazza, F., Roediger, E., & Brüggen, M. 2012, *A&A*, 544, A103, doi: [10.1051/0004-6361/201118688](https://doi.org/10.1051/0004-6361/201118688)

Vega-García, L., Perucho, M., & Lobanov, A. P. 2019, *A&A*, 627, A79, doi: [10.1051/0004-6361/201935119](https://doi.org/10.1051/0004-6361/201935119)

Vernstrom, T., Gaensler, B. M., Rudnick, L., & Andernach, H. 2019, *ApJ*, 878, 92, doi: [10.3847/1538-4357/ab1f83](https://doi.org/10.3847/1538-4357/ab1f83)

Weżgowiec, M., Jamrozy, M., Chyży, K. T., et al. 2024, *A&A*, 691, A193, doi: [10.1051/0004-6361/202451580](https://doi.org/10.1051/0004-6361/202451580)

Wing, J. D., & Blanton, E. L. 2011, *AJ*, 141, 88, doi: [10.1088/0004-6256/141/3/88](https://doi.org/10.1088/0004-6256/141/3/88)

—. 2013, *ApJ*, 767, 102, doi: [10.1088/0004-637X/767/2/102](https://doi.org/10.1088/0004-637X/767/2/102)

Yang, X., Joshi, R., Gopal-Krishna, et al. 2019, *ApJS*, 245, 17, doi: [10.3847/1538-4365/ab4811](https://doi.org/10.3847/1538-4365/ab4811)